

Near Islands Aleutian Earthquake with $M_W = 7.8$ on July 17, 2017: I. Extended Rupture along the Commander Block of the Aleutian Island Arc from Observations in Kamchatka

D. V. Chebrov^{a, b}, Yu. A. Kugaenko^{a, *}, A. V. Lander^c, I. R. Abubakirov^a, A. A. Gusev^{a, c, †},
S. Ya. Droznina^a, S. V. Mityushkina^a, D. A. Ototyuk^a, V. M. Pavlov^a, and N. N. Titkov^a

^a*Kamchatka Branch, Federal Research Center Geophysical Survey of Russian Academy of Sciences,
Petropavlovsk-Kamchatskii, 683006 Russia*

^b*Schmidt Institute of Physics of the Earth, Russian Academy of Sciences, Moscow, 123242 Russia*

^c*Institute of Earthquake Prediction Theory and Mathematical Geophysics,
Russian Academy of Sciences, Moscow, 117997 Russia*

^d*Institute of Volcanology and Seismology, Far Eastern Branch, Russian Academy of Sciences,
Petropavlovsk-Kamchatskii, 683006 Russia*

*e-mail: ku@emsd.ru

Received April 26, 2018; revised August 18, 2018; accepted December 3, 2018

Abstract—The largest instrumentally recorded regional back-arc earthquake with $M_W = 7.8$, $M_C = 8.2$ occurred on July 17, 2017 on the Bering transform fault (the boundary between the Beringia minor lithospheric plate and the Komandorskii (Commander) block of the Aleutian island arc). This seismic event, called the Near Islands earthquake or Near Islands Aleutian earthquake, caused the ground to shake with intensity $I = 5–6$ on Bering Island and a small tsunami wave on the Near Islands. The specific aspects of the peculiarities of the pattern of seismicity of the northwestern segment of the Aleutian arc and the tectonic position of the Near Island Aleutian earthquake, the details of its prompt processing, macroseismic manifestations, analysis results of ground motion peak amplitudes, focal mechanisms, and earthquake source models are discussed. The coseismic displacements according to the GNSS data are presented. It is concluded that the source of the Near Islands Aleutian earthquake did not fill the seismic gap near the Commander Islands, and the possibility of the strongest earthquake hitting the northwestern part of the Aleutian arc remains.

Keywords: earthquake, Bering Fault, Commander segment of the Aleutian arc, tsunami, focal mechanism, coseismic displacements, coseismic deformation, peak ground motion

DOI: 10.1134/S1069351319040037

INTRODUCTION

The earthquake of July 17, 2017 called the Near Islands Aleutian earthquake (NIAE) (Chebrov et al., 2017b) occurred in the Commander segment of the Aleutian island arc (Figs. 1–3, Table 1). The source area of the earthquake stretched ~5000 km along the northeastern (sloping towards the Bering Sea) edge of the arc partially also capturing its axial areas. The ground shaking from this earthquake was felt on the Bering Island with intensity $I = 5–6$ on MSK-64 scale.

The NIAE is located in the zone of a geodynamic analog of the Sumatra $M_W = 9.1$ earthquake of December 26, 2004 (Lander et al., 2009; Gordeev et al., 2015, etc.). The importance of studying the NIAE is determined by its closeness to the region of relative seismic quiescence in the western part of the Aleutian arc: this

earthquake occurred at the boundary of the Commander seismic gap (Sykes, 1971; Lobkovskii et al., 2014; Gordeev et al., 2015; and Gussyakov, 2018) whose size is unclear but, in the opinion of some authors, e.g., (Lobkovskii et al., 2014), corresponds to the source of an earthquake with $M \sim 9.0$. As has been already noted in (Chebrov et al., 2017b), the cloud of the aftershocks and the region of seismic quiescence are spatially distant from each other; nevertheless, it is quite probable that the NIAE resulted in the changes in the seismotectonic stress field in the region of the seismic gap.

Extensive new seismological and geophysical data have been acquired and analyzed in connection with the NIAE. During seven months after this earthquake, more than 900 seismic events, most of them being the NIAE aftershocks, were localized in the northwestern part of the Aleutian arc. The extent of the cloud of NIAE aftershocks is severalfold larger than the typical linear size of a source of the subduction and continen-

† Deceased.

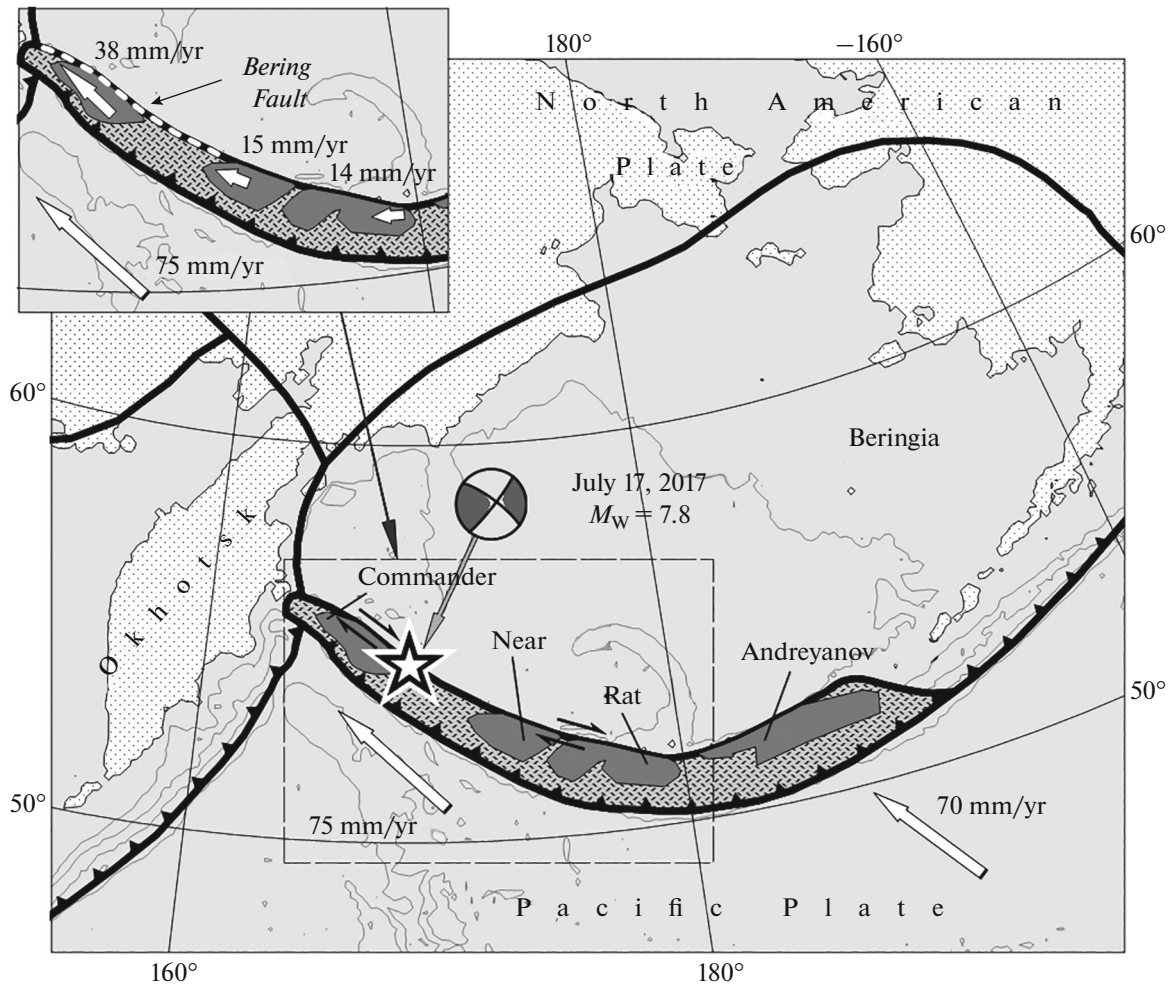


Fig. 1. Mosaic of minor plates and blocks in northern Pacific. Heavy black lines are plate boundaries. Relatively rigid segments of the arc—Commander, Near, Rat, and Andreyanov blocks—are shown in solid gray. Rest of arc presumably with predominant arc-parallel extension and lower coupling with underlying submerging plate is dark speckled. Heavy light arrows indicate direction and velocities of motion of Pacific Plate according to NNR_NUVEL1A model (Argus, Gordon, 1991). Asterisk marks NIAE epicenter. White arrows in inset show directions of motion of individual rigid blocks of Aleutian arc and values of arc-parallel velocity components (Cross and Freymueller, 2008). All velocities are relative to North American Plate.

tal earthquakes with $M \approx 7.7-7.8$. The foreshock activity lasted for about 11 months—starting from September 2016. The coseismic displacements from this earthquake were detected by the GNSS¹ stations within a radius of ~ 1000 km from the epicenter. Macroseismic and strong motion data have been collected and systematized for this earthquake. The models of the slip in the NIAE source are being developed. The sequence of the seismic events that accompanied the NIAE in the region of the Commander block has a certain similarity with the scenario of the development of the Sumatra mega-earthquake with $M_w = 9.1$ on December 26, 2004.

The results of our studies of the NIAE are synthesized in an integrated paper which is divided into two

¹ GNSS (Global Navigation Satellite Systems) is the common name for satellite navigation systems.

parts because of the large volume of the material. In the first part, we discuss the tectonic position of the NIAE, its focal mechanism and source models, coseismic displacements, the analysis of the ground motion waveforms, and specific aspects of operative data processing. The second part addresses the analysis of the foreshock–aftershock process of this strong earthquake. The presented results of our studies are mainly based on the data obtained by the Kamchatka system for seismological and geophysical monitoring KAGSR (in particular, in the Kamchatka regional earthquake catalog²). Also, the data of the world seis-

² Kamchatka Branch of Federal Research Center Geophysical Survey of Russian Academy of Sciences, Seismological Data Information System, regional catalog of Kamchatka and Commander Islands. <http://www.emsd.ru/sdis/earthquake/catalogue/catalogue.php>

mological information centers (MOS, NEIC, ISC, IDC)³ were used. The focal mechanisms of the earthquakes were analyzed based on the GCMT⁴ catalog. The seismic moment tensor of NIAE was calculated from the IRIS, ARN, and JP⁵ broadband seismic network data accessible via the IRIS DMC data center⁶.

TECTONIC POSITION OF THE EARTHQUAKE AND PATTERN OF SEISMICITY OF THE NORTHWESTERN SEGMENT OF THE ALEUTIAN ISLAND ARC

The region hit by the earthquake is adjacent to the boundary between the Pacific and North American largest lithospheric plates which stretches along the Aleutian oceanic trough. Here, one of the most active seismic zones accommodating numerous earthquakes with magnitudes up to $M \approx 8-9$ is located (Ruppert et al., 2007, Balakina and Moskvina, 2010). The present-day tectonic activity of this zone is due to the high velocity of relative displacements of the interacting plates, which varies approximately within 60–75 mm/yr along the length of the Aleutian arc (hereinafter, the plate and block velocities are presented relative to the North American Plate).

In the region under consideration, the main rigid massifs of the Pacific and North American plates do not directly contact each other but interact through a series of small boundary plates and blocks (Fig. 1). The boundaries between them are at places traced by the linear zones of the earthquakes; at the same time, areas of scattered seismicity are also widespread. According to the ISC, the earthquakes that occur on these interblock boundaries can have magnitudes above 7.5. The largest boundary block is the Beringia Plate occupying almost the whole Bering Sea area and some coastal regions (Lander et al., 1994; Mackey et al., 1997; Gordeev et al., 2015).

Along its southern edge, Beringia is skirted by the Aleutian Island arc. Following (Geist et al., 1988), several separate relatively large elevated blocks are distinguished in its central and western parts. Among these blocks, the Andreyanov, Rat, and Near blocks

named after the corresponding islands are the main ones. This series should be complemented by the westernmost Commander block (Fig. 1). The southern (facing the Aleutian trench) slopes of the blocks and the relatively subsided interblock segments have a complicated topography with numerous spurs and canyons where the faults are identified oblique or transverse to the main strike of the arc. In contrast, in the north, the considered area is bounded by a series of the extended arc-parallel troughs and lineaments which are right-lateral strike-slips as suggested by the focal mechanisms (Fig. 2, inset).

According to the GNSS data (Cross and Freymueller, 2008), large blocks are moving along the arc toward the west (Fig. 1, inset). The respective velocity components for the three eastern blocks are at most 15 mm/yr. These velocities are small compared to the relative motion of the Pacific Plate; therefore, most of the boundary blocks (including Beringia and Aleutian arc) are in the first approximation frequently attributed to the North American Plate. The Commander block whose kinematics is closer to the Pacific Plate is the exception. The Pacific Plate in this region moves northwest at about 75 mm/yr (Argus and Gordon, 1991). The Commander block moves in the same direction but with a lower velocity of ~40–50 mm/yr (Levin et al., 2012; Cross and Freymueller, 2008; Kogan et al., 2017). Thus, the Commander block fairly rapidly drifts in the same direction relative to the slow Beringia (satisfactory estimates of its velocity are absent).

The motion of the different parts of the arc along its strike is the result of the oblique subduction of the Pacific Plate. In (Ryan and Scholl, 1993) it is hypothesized that large blocks are relatively strongly coupled with the descending slab and are sliding along the arc under the action of the tangential component of the subduction. Due to the bend of the arc, the tangential component increases towards the west and, as a consequence, the displacement velocity of the blocks of the hanging also increases in the same direction (Fig. 1, inset). As a result, the arc experiences arc-parallel extension (McCaffrey, 1992; Lallemand and Oldow, 2000). These deformations are implemented, primarily, in the regions separating the large blocks where the coupling with the underlying slab is assumed to be slower. The extension also explains the relative subsidence and crushing of the interblock regions.

The NIAE is likely to be directly related to arc-parallel movements of the blocks of the Aleutian arc. The earthquake occurred on the Bering Fault, which extends for ~700 km, is clearly expressed in the submarine topography (Seliverstov, 1998; Gaedicke et al., 2000), and composes the northeastern boundary of the Commander block. Elongated in the direction of motion, the narrow Commander block has two sub-parallel active boundaries: the southwestern boundary running along the Aleutian trench and the northeastern boundary along the Bering Fault. The movements

³ Information centers: MOS: Federal Research Center Geophysical Survey of Russian Academy of Sciences, Obninsk (www.gsras.ru); NEIC: National Earthquake Information Center, U.S. Geological Survey <https://earthquake.usgs.gov/earthquakes/search/>; ISC: Bulletin of the International Seismological Centre. <ftp://ftp.isc.ac.uk/pub/isc/catalogue/> ISC-GEM: Global Instrumental Earthquake Catalogue (1904–2014). <http://www.isc.ac.uk/iscgem/index.php> IDC: International Data Centre, Comprehensive Nuclear-Test-Ban Treaty Organization (CTBTO), Vienna, Austria (www.ctbto.org).

⁴ GCMT is the Global CMT Project (www.globalcmt.org).

⁵ Broadband seismic station networks: IRIS: Global Seismograph Network GSN–IRIS/USGS (<https://doi.org/10.7914/SN/IU>); ARN: Alaska Regional Network (<https://doi.org/10.7914/SN/AK>); JP: Japan Meteorological Agency Seismic Network (<http://www.fdsn.org/networks/detail/JP/>).

⁶ <http://ds.iris.edu/wilber3/>

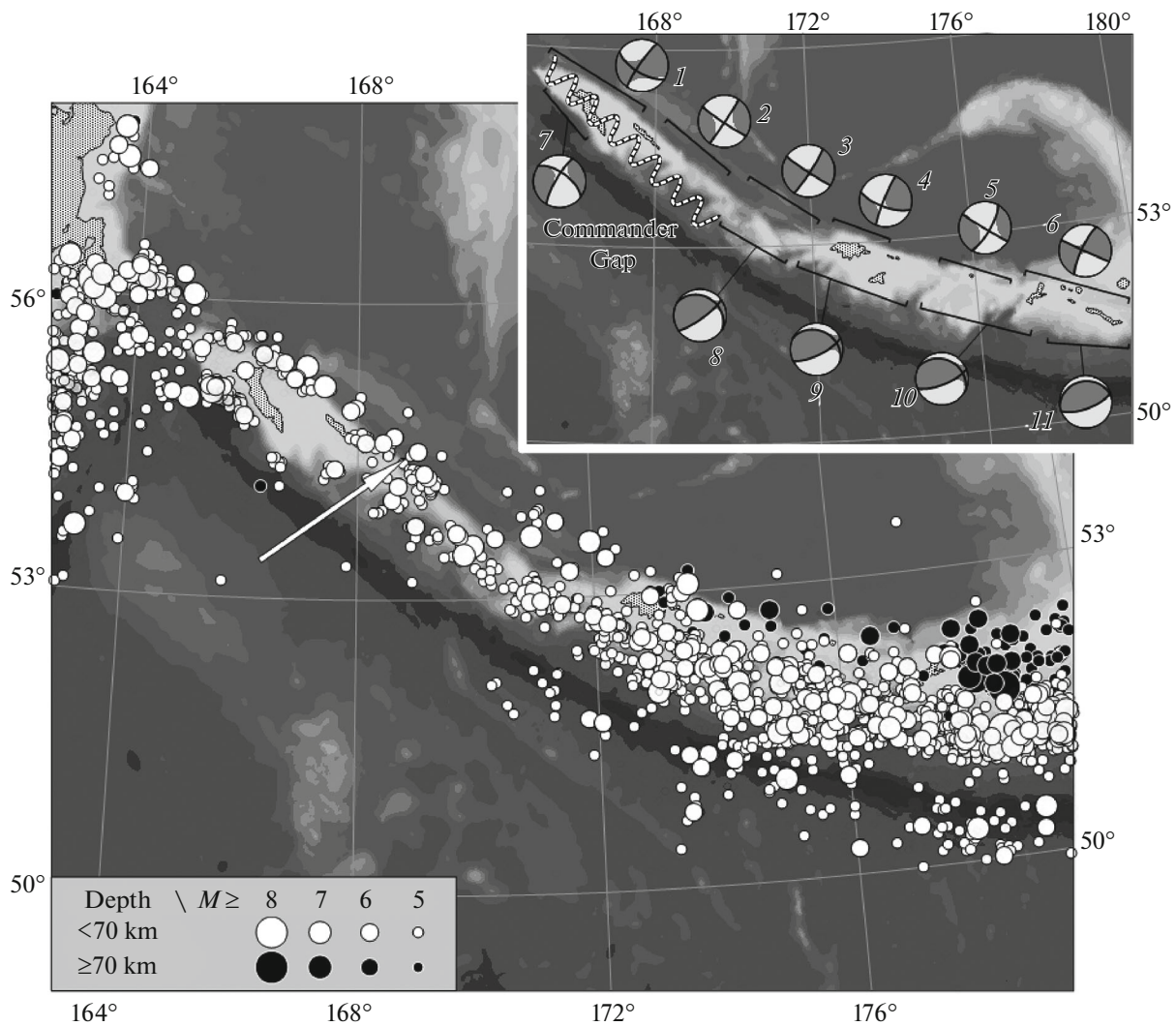


Fig. 2. Earthquakes with $M \geq 5$ in western part of Aleutian arc recorded before beginning of NIAE aftershock process according to ISC (1903 to 2014) and NEIC catalogs (January 2015 to August 2016). White arrow indicates position of NIAE epicenter. Inset shows diagrams of mean normalized seismic moment tensors calculated from GCMT catalog data (1977 to August 2016) for different segments of northern and southern slopes of Aleutian arc. Earthquake statistics on arc segments: segment 1, 19 events; segment 2, 21 event; segment 3, 8 events; segment 4, 5 events; segment 5, 7 events; segment 6, 13 events; segment 7, 15 events; segment 8, 19 events; segment 9, 27 events; segment 10, 49 events; segment 11, 83 events. Spring sign marks approximate position of Commander seismic gap whose size is debatable.

on both boundaries are right-lateral strike slips which is confirmed by the mechanisms of numerous earthquakes (the diagrams of the mean seismic moment tensor for the respective segments of the arc are shown in the inset in Fig. 2). This model of the Commander block's motion is also supported by the GNSS data (Kogan et al., 2017). The mechanism of the NIAE is also the right-lateral strike slip. The cloud of NIAE aftershocks in its southeastern part not only spans along the Bering Fault but also captures the entire arc body, including the extension zone which separates the Commander block from the next large block of the Near Islands (Fig. 3). Here, the aftershock activity can probably be associated with the movements of the underlying slab.

Figure 2 illustrates the seismicity of the western part of the Aleutian arc according to the ISC and NEIC world catalogs from 1903 to August 2016, i.e., over the entire instrumental period before the beginning of the NIAE aftershock process. The detailed review of the present and historical seismicity of the Aleutian arc is presented in (Balakina and Moskvina, 2008; 2009; 2010a; 2010b).

The main Commander block encompassing the shelf down to a depth of 200 m with the Bering and Mednyi islands is located between two zones of shallow-focus seismicity skirting the Aleutian trench in the southwest and the Bering Fault in the northeast. The earthquakes with $M \sim 7$ are reliably detected in both

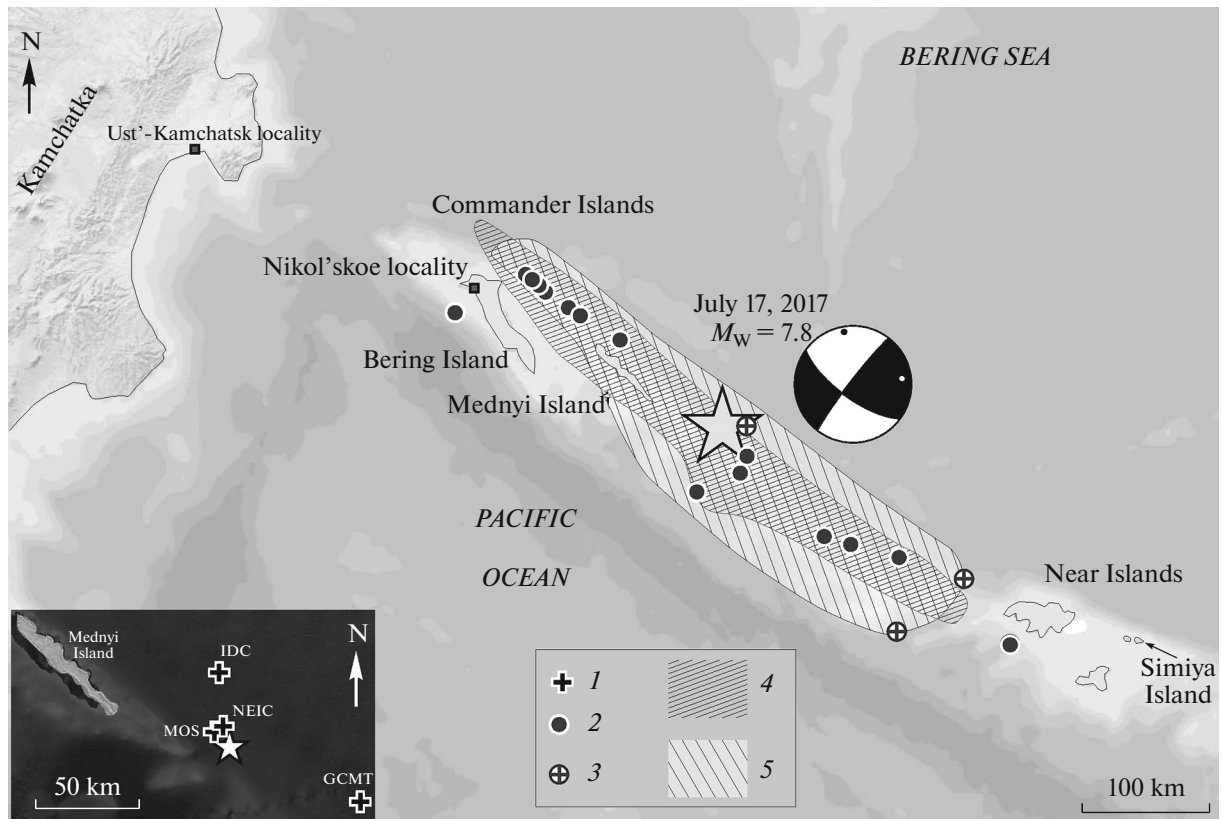


Fig. 3. Source area of Near Island Aleutian earthquake. Inset shows NIAE epicenter according to KAGSR data (asterisk) in comparison with data from other data centers (1). Epicenters of NIAE aftershocks with $M > 5.0$ according to KAGSR (2) with additions according to NEIC (3) are indicated. Hachure marks first-day aftershock area according to KAGSR (4) and NEIC (5). Stereogram of focal mechanism of NIAE according to KAGSR (Table 4) is presented.

zones. Several stronger events presented in the catalogs correspond to the early observation period and may pertain to the adjacent regions. Generally, during the period of instrumental observations, the northeastern boundary behaves more actively than the southwestern one.

Relative seismic quiescence, particularly clearly pronounced for the strongest events, is observed

within the Commander Block and south of it; therefore, the region is considered a seismic gap (Sykes, 1971; McCann et al., 1979; Lobkovskii et al., 2014; Gussyakov, 2018) (Fig. 2, inset). Attention has been repeatedly drawn to the analogy of the Commander segment of the Aleutian arc and the northwestern part of the Sunda subduction zone, the region of the stron-

Table 1. Main parameters of Near Island Aleutian earthquake of July 17, 2017 according to KB GS RAS regional data (KAGSR information processing center) and determinations by other information processing centers

Data Center	t_0 , h min s	Hypocenter			Magnitude class
		φ° , N	λ° , E	h , km	
KAGSR	23:34:08.1	54.35	168.90	7	K_S 16.1*; M_L 7.3; M_W 7.8; M_C 8.2
MOS	23:34:10.90	54.43	168.82	10	m_b 7.0; M_S 7.5
NEIC	23:34:13.74	54.443	168.857	10	M_W 7.7; m_b 6.8; M_{S20} 7.7
IDC	23:34:12.52	54.657	168.817	0	M_S 7.5
GCMT**	23:34:57.7	54.13	169.78	23	M_W 7.8

* K_S is energy class according to classification of S.A. Fedotov (Fedotov, 1972); ** Centroid parameters. Magnitudes: m_b is based on amplitude of P -wave measured by short-period instruments; M_W is moment magnitude; M_S is surface wave magnitude; M_{S20} is magnitude based on surface waves measured at period of ~ 20 s; M_L is local magnitude; M_C is coda wave magnitude.

gest Sumatra earthquake of 2004⁷ (McCaffrey, 1992; Lander et al., 2009). The Sunda analogs are 2–2.5 times as large as the Commander structure linearly and ~5 times as large in terms of area. Based on these values and the empirical relations linking the source size and magnitude of a seismic event (Kanamori and Andersen, 1975), the magnitude of the potentially strongest Commander earthquake can be estimated at 8.1–8.4. The fact that the western part of the Aleutian arc is prone to a much stronger earthquake than all the previously known ones calls for special attention to this region.

Approximately 50 km southeast of Mednyi Island, the northeastern branch of the seismicity of the Commander Block turns south, passes to the arc's southern slope, and merges with the southwestern branch. Further southeast, within the relatively subsided part of the arc, the band of the densest concentration of the earthquakes gradually migrates from the arc axis towards the Aleutian trench. Besides the main band of seismicity localization, shallow-focus events are detected here all over the entire body of the arc and in its vicinity. In particular, several strong earthquakes with $M \sim 7$ perhaps occurred in the back-arc basin.

Due to the fact that the main band of previous seismicity east of the Commander Islands is drifting southwards, the southeastern part of the Bering Fault during the period prior to the NIAE was less active than the northwestern part (Fig. 12a). Since 1962 (when the accuracy of hypocenter determination became sufficiently high to allow a reliable correlation of the seismic events to the movements on the fault) to the middle of 2017, the ~300-km segment of the Bering Fault which borders the Commander Block in the northeast accommodated 14 earthquakes with $M_w \geq 5.5$ excluding two aftershocks. During the same period, only three earthquakes of the same magnitudes (excluding one aftershock) occurred on the remaining ~200-km segment of the fault. We note that the boundary between the mentioned active and passive segments of the Bering Fault are located as close as 20–30 km to the NIAE epicenter. Below we discuss the assumption that the NIAE main rupture corresponded to the slip along the southeastern, previously relatively locked segment of the Bering Fault.

In contrast to the eastern part of the Aleutian arc where the seismicity clearly reflects the motions in the subduction zone the situation in the west is more complicated. The descending plate is traced by the presence of the sloping seismofocal zone up to the Near Islands in the west. The maximal depth of the earthquakes decreases accordingly to 120 km (from the maximal depths 300–400 km east of the Rat Islands

according to the IGC data). As noted above, the indirect GNSS data suggest that the tilted submerged slab of the Pacific Plate can probably extend even further northwest underlying the Commander block of the Aleutian Arc. Moreover, in this case, from the kinematic standpoint, the slab should move parallel to the arc without further submergence. However, west of the Near Islands at the transition to the Commander block, only separate earthquakes at intermediate depths ~100 km are detected. Because of the insufficiently accurate determination of hypocenters (primarily, hypocentral depths), it is impossible to track the presence of the Pacific Plate's continuation beneath the Commander Block based on the seismicity data.

The focal mechanisms of the earthquakes with the epicenters on the southwestern slope of the Aleutian Arc within the segment between the Near and Commander islands, i.e., in the upper part of the assumed western continuation of the subduction zone is yet another fairly convincing, albeit, indirect argument supporting the existence of the submerged Pacific slab beneath the Commander block. These earthquakes characteristically have focal mechanisms with the fault planes gently plunging beneath the arc and the right-lateral strike slips with a small reverse fault component (segments 8 and 9 in the inset of Fig. 2). This pattern is closely consistent with the kinematics of oblique subduction for the assumed continuation of the submerged part of the Pacific Plate on the segment of the bend of the Aleutian Arc between the Near and Commander islands. The cloud of the NIAE aftershocks is not confined to the vicinity of the Bering Fault but partially spans south into this region. It is likely that as a result of the main shock, also the adjacent segments of the zone of oblique subduction were activated. Moreover, among the strong aftershocks of the NIAE there was also the event from this zone with the mechanism of oblique subduction (January 7, 2018, $M_w = 5.2$), which emphasizes the close interaction of the two regions.

These tectonic notions were used in the interpretation of the data obtained by the KAGSR presented below.

PROCESSING THE EARTHQUAKE AT THE REGIONAL INFORMATIONAL- PROCESSING CENTER (IPC) PETROPAVLOVSK

The NIAE, its foreshocks, and its aftershocks were processed at the informational-processing center (IPC) Petropavlovsk based on the records by seismic stations located on the Kamchatka Peninsula, in the Far East of Russia, and in the territories of neighboring countries, from which the data are accessible at the IPC in real-time (Fig. 4). Seventy-eight of these stations pertain to the Kamchatka regional network (Chebrov et al., 2013; 2017a). The Bering station (BKI) located on the Bering Island is closest to the NIAE epicenter (the epicentral distance Δ is ~200 km).

⁷ USGS, Earthquake Hazards Program, 2004. M 9.1 off the west coast of northern Sumatra. https://earthquake.usgs.gov/earthquakes/eventpage/official20041226005853450_30#executive; <https://earthquake.usgs.gov/archive/product/poster/20041226/us/1457989040172/poster.pdf>

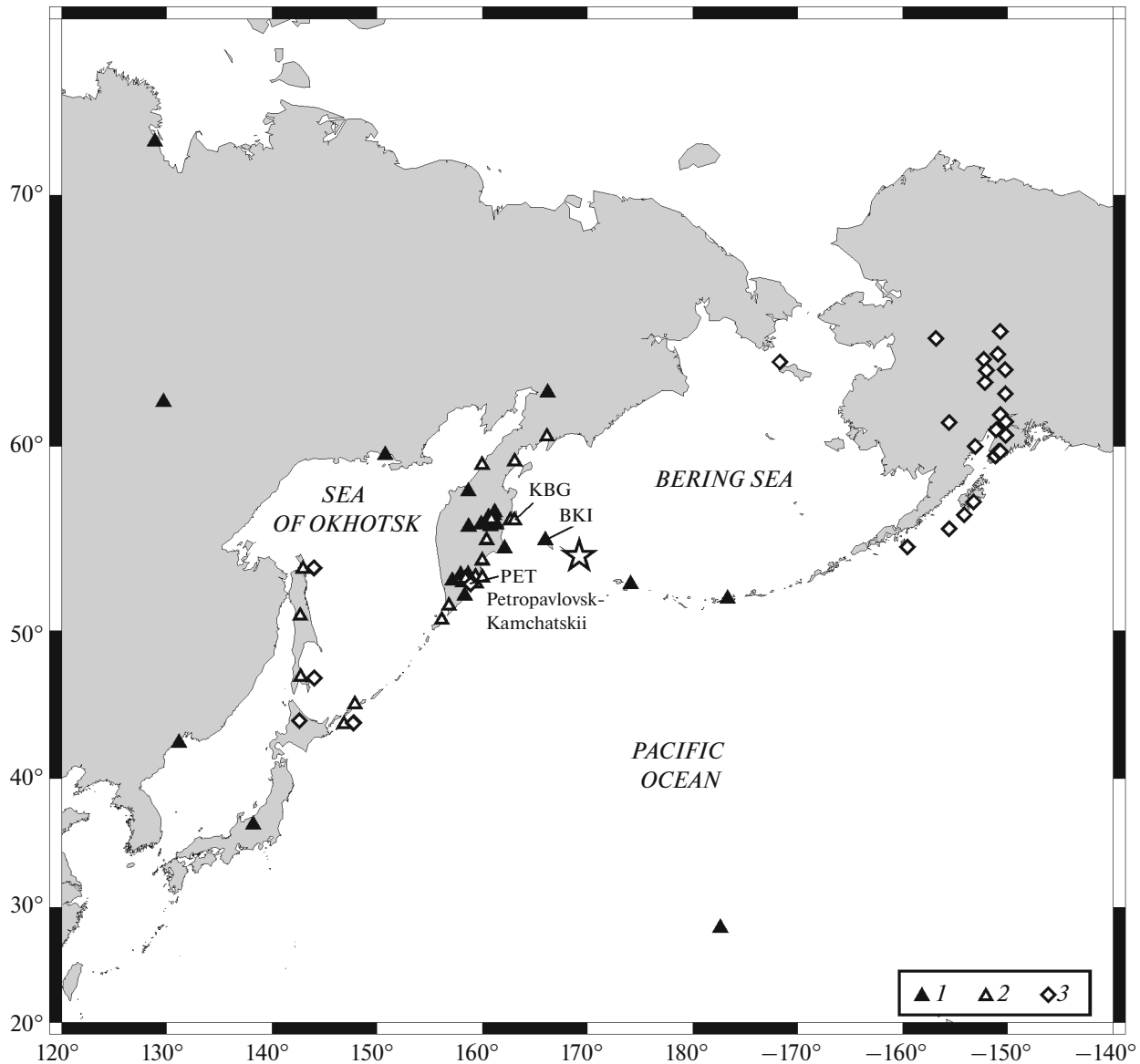


Fig. 4. Seismic stations used in IPC Petropavlovsk for processing NIAE, its foreshocks, and its aftershocks (1), including those used for determining peak amplitudes of ground motion (2). Stations used for calculating SMT are indicated (3). Station names are presented for stations mentioned in text.

IPC Petropavlovsk operates in continuously round-the-clock following the regulations of the Tsunami Warning System (TWS) for events with $M \geq 6.0$ and the Urgent Message Service (UMS) for events with $M \geq 5.0$, and it monitors all the strong earthquakes of the Russian Far East. According to the current TWS regulations, seismic alerts are based on the magnitude–geographical criterion: a tsunami warning is issued for the undersea earthquakes when the magnitude of an event exceeds 7.0. As of now, the reference magnitude for IPC Petropavlovsk has been the surface wave magnitude M_S (PET) determined by the Petropavlovsk (PET) station. According to the TWS regulations, processing a potentially tsunamigenic earth-

quake ($M \geq 6.0$) detected within 1000 km from IPC Petropavlovsk should not take more than 10 min.

The duty staff of IPC started processing the NIAE immediately after the alarm was released when the recorded seismic signal exceeded the given threshold at the Bering (BKI) station. The actions of the operators during the work on processing the earthquake fully complied with the requirements of the existing regulations (Table 2). According to the magnitude–geographical criterion, the NIAE parameters corresponded to the potentially tsunamigenic earthquake (located beneath the Bering sea, shallow hypocentral depth, magnitude M_S (PET) = 7.6); therefore, the tsunami warning was issued. According to the Pacific

Table 2. Synopsis of NIAE processing at IPC Petropavlovsk according to TWS and UMS regulations

Time	Events and actions of duty operators	Note
23:34:43	<i>P</i> -wave arrival at Bering station (BKI). Alarm activation	Duty staff began processing earthquake
23:35:00	Transmitting “Strong earthquake is recorded” signal	Informing Kamchatka observation center and tsunami warning by Kamchatka Department of Hydrometeorology Survey
23:35:43	<i>P</i> -wave arrival at Petropavlovsk station (PET)	
23:37:01	<i>S</i> -wave arrival at PET station	
23:37:50	First determination of earthquake source region and first estimation of energy from PET station data	Epicentral distance $\Delta = 6.8^\circ$ (~750 km from Petropavlovsk–Kamchatskii) Lat = 53.99° N, Lon = 169.72° E, $H = 16$ km, $MPSP$ (PET) = 7.0, $K_p = 13.2$ Origin time 23:34:00.8
23:42:32	Updating estimates of earthquake parameters	Lat = 53.9° N, Lon = 169.9° E, $H = 6$ km, M_S (PET) = 7.6, M_S (20R) = 7.5, $K_p = 13.2$ Origin time 23:33:58.2
23:44:09	Transmitting tsunami alarm signal (form nos. 2, 2a) according to approved distribution list to Central Telegraph, Main Department of Ministry of Russian Federation for Civil Defence, Emergencies and Elimination of Consequences of Natural Disasters (EMERCOM) for Kamchatka krai; Kamchatka Observation and Tsunami Warning Center of the Kamchatka Department of Hydrometeorology Survey; Administration of Kamchatka krai; regional administrations of Kamchatka krai, etc.	Tsunami warning is issued according to magnitude–geographical criterion: location beneath seafloor of Bering Sea, shallow hypocentral depth, magnitude M_S (PET) = 7.6
23:51:00	Estimating ground shaking intensity at localities based on instrumental data (records by accelerometers of Kamchatka regional network (Droznin et al., 2017))	Informing Ministry of Russian Federation for Civil Defence, Emergencies and Elimination of Consequences of Natural Disasters (EMERCOM) for Kamchatka krai

Tsunami Warning Center⁸ bulletin, the tsunami wave was instrumentally recorded on Simiya (Shemya) Island, the Near Islands, where its height was ~0.1 m. In the open ocean, at the nearest DART⁹ station located ~500 km from NIAE epicenter, the tsunami wave at the estimated arrival time was also at most ~0.1 m. According to the data of the Tsunami Center of the Kamchatka Department of the Federal Service for Hydrometeorology and Environmental Protection (Rosgidromet), no tsunami waves were observed on the Kamchatskii krai coast.

Final processing of NIAE was carried out based on the data from 55 seismic stations. The determination error was 10 km for the epicenter and 24 km for the

depth. The hypocenter calculated at the Kamchatka Branch of the Geophysical Survey of Russian Academy of Sciences (KB GS RAS) is consistent with the determinations by the other information processing centers (Table 1, Fig. 3). The NIAE epicenter is located at the Bering Fault on the Bering Sea’s continental slope southeast of Bering Island. The position of the centroid (according to GCMT data) is shifted ~60 km southeast relative to the instrumentally determined epicenter.

MACROSEISMICITY

The NIAE epicenter was located ~200 km southeast of the Nikol’skoe locality on Bering Island where the intensity I of ground shaking was up to 5–6 on the MSK-64 scale (Medvedev et al., 1965). The prompt intensity estimate ($I_{\text{calc}} = 5.5$) calculated from the instrumental data (Droznin et al., 2017) agrees fairly

⁸ <http://www.tsunami.gov/events/PAAQ/2017/07/17/ot9dh6/2/WEAK51/WEAK51.txt>

⁹ http://www.ndbc.noaa.gov/download_data.php?filename=21415t2017.txt.gz&dir=data/historical/dart/

closely with the reports from local people. The earthquake was felt by all the residents of Nikol'skoe; many were frightened and left the premises. An underground rumble was heard. Many people felt giddy and sick, it was difficult to keep their footing; some, losing their balance, held on to stable objects. Pet animals were worried and ran outdoors. The earthquake lasted for about 2 min: initially there was a strong progressive shaking, followed by smooth vibrations affecting the coordination. No casualties or damage was detected.

On the Kamchatka Peninsula, the earthquake was felt less intensively, with intensity $I \approx 3-4$ in the region of the Ust'-Kamchatsk locality (epicentral distance $\Delta \sim 450$ km), $I \approx 4$ at the Kronoki cordon ($\Delta \approx 500$ km), $I \approx 2-3$ in Petropavlovsk-Kamchatskii ($\Delta \approx 690$ km), and $I \approx 1-2$ in the Atlasovo locality ($\Delta \approx 600$ km) (Fig. 5).

During seven months after the NIAE, 36 perceptible aftershocks occurred. They produced ground shaking which was felt in the Nikol'skoe locality ($\Delta \sim 20-260$ km) with the intensity ranging from 2 to 5-6. Twenty-three of these earthquakes occurred in January 2018. Ground shaking with intensity 5-6 ($\Delta \sim 50$ km) was caused by the strongest NIAE aftershock with $M_w = 6.2$ detected on January 25, 2018 in the northwestern part of the source zone.

ANALYSIS OF GROUND MOTION PEAK AMPLITUDES

The ground motion data from the NIAE drew a great deal of interest because the strong ($M_w = 7.7-7.8$) earthquake with the epicenter on the Bering Fault is an important event in the recent seismicity in Kamchatka. In this work, we carried out a preliminary analysis of the peak amplitudes of the ground motion from this earthquake (Table 3).

The seismic stations that were used in the analysis of strong motion from the NIAE are shown in Fig. 4. Unfortunately, the operation of the BKI station at Nikol'skoe, Bering Island, which is the closest station to the epicenter, was interrupted by the ground shaking.

The stations are equipped with digital accelerometers (channel code NH*) and/or velocimeters (channel codes BH*, BL*). The instruments mainly have sensors manufactured by Guralp, Britain (CMG-5TD, CMG-6TD, and CMG3TB modifications) with a sampling frequency of 100 Hz (Chebrov et al., 2013). The records were processed with the use of the program package briefly described in (Chebrov et al., 2013). An illustration is presented in Fig. 6 showing the graphs of the ground motion at the Krutoberegovo station (KBG). The peak values are 3.5, 3.2, and 1.9 cm/s² for accelerations in the EW, NS, and Z components; similarly, 1.5, 3.1, and 1.2 cm/s for the velocity and 2.7, 7.5, and 2.6 cm for the displacements.

Figure 7 illustrates the pattern of the attenuation of the peak amplitudes with hypocentral distance r for the main shock. The peak accelerations are shown in

Fig. 7a. For comparison, we present the graph of the attenuation of the peak amplitudes of the horizontal acceleration for the earthquake with $M_w = 7.7$ according to the decay law for the Japanese earthquakes based on the formula from (Fukushima and Tanaka, 1992) (in this formula, ground conditions are disregarded).

Figure 7b shows the peak velocities. For comparison, we present the calculated graph of the attenuation with distance for peak velocity in the horizontal channels according to the calibration curve for Fedotov's energy class K^{F68} (Fedotov, 1972) with the actual value $K^{F68} = 16.1$. Since this calibration curve describes the behavior of parameter A/T , for comparison, its values were multiplied by 2π . The points fall noticeably higher than we expected from the calibration curve. This discrepancy can probably be explained in the following way. The considered records of a broadband digital velocigraph (or their emulation by the record of a digital accelerograph) soundly fix the maximal amplitudes of the group of surface waves with periods of 11-13 s (this spectral peak is distinctly seen in the Fourier spectra of the velocity). At the same time, the K^{F68} value is calculated with the use of a signal that has an artificially limited frequency band simulating the record of the 1.2-s VEGIK seismograph. Emulation of the VEGIK record with the use of broadband digital records is a necessary step for calculating K^{F68} . Discrepancies of this kind arise even for moderate magnitudes of 4 to 5, whereas in the case of $M_w = 7.7$, they reach one order of magnitude, as seen in Fig. 6b. The qualitative consistency between the trend of the observed data and the trend of the calibration curve is reasonably good.

The preliminary analysis of the NIAE ground motion amplitudes suggests the following tentative conclusions:

- the level of peak amplitudes of the acceleration in the range of the distances from 400 to 800 km is commensurate with the level expected for the typical earthquakes of Japan;

- the attenuation with distance for peak velocities in the range of distances from, 500 to 700 km is steeper than for the calibration curve of Fedotov's energy class K^{F68} scale;

- the level of peak velocities for the actual magnitude $M_w = 7.7$ is significantly (by a factor of about ten) higher than the level calculated from the A/T value for the actual K^{F68} value. This fact agrees with the significant difference in the operating frequency bands of the broadband digital logger, on one hand, and the emulated analog instrument VEGIK, on the other hand.

FOCAL MECHANISM

Recently, the focal mechanisms of regional earthquakes are calculated at KB GS RAS with the use of

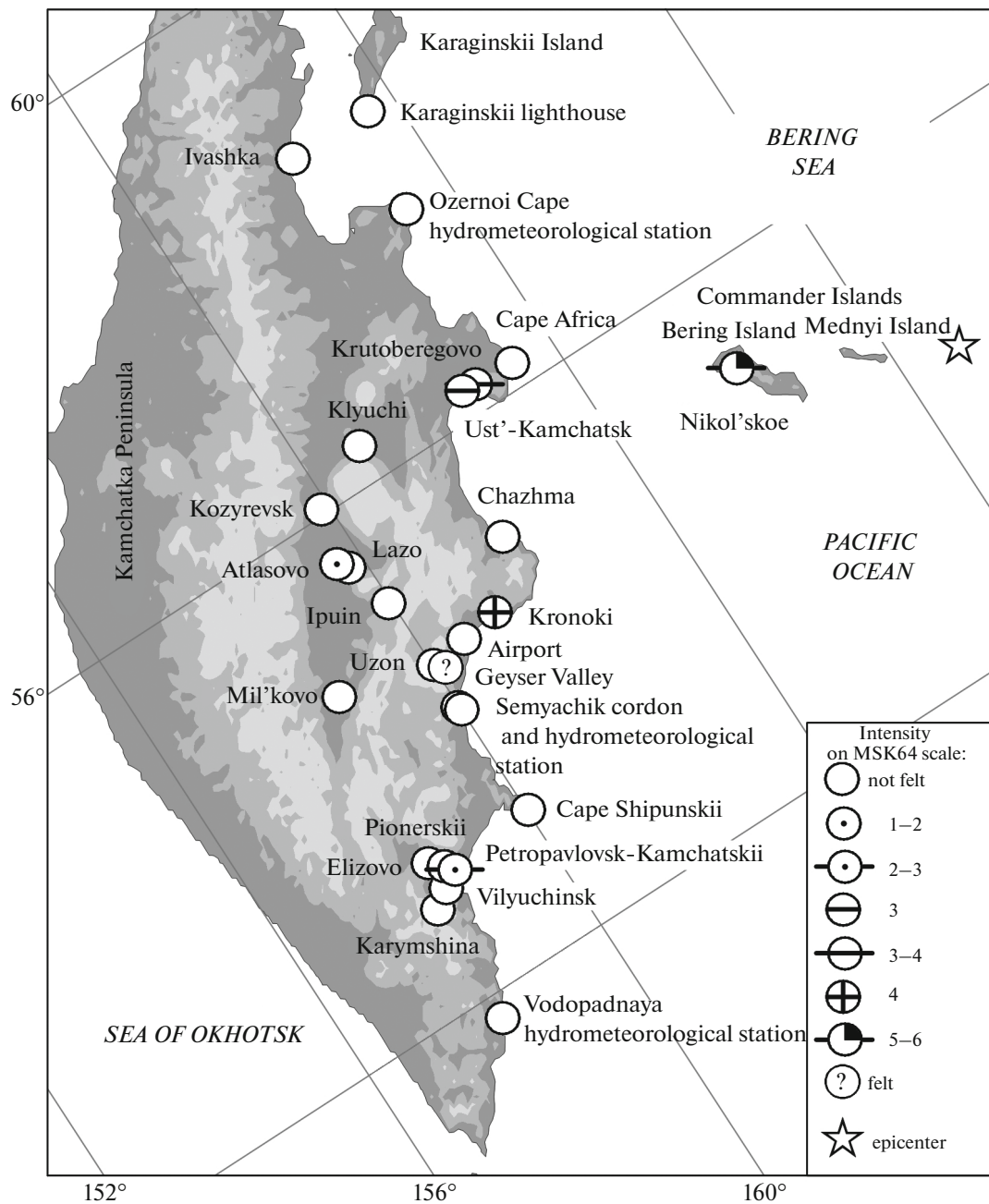


Fig. 5. Map of macroseismic manifestations of NIAE in territory of Kamchatskii krai.

the approach based on the seismic moment tensor (SMT) determination by the technique described in (Pavlov and Abubakirov, 2012; Abubakirov et al., 2015). This method was used for identifying the NIAE focal mechanism. The initial data were the waveforms recorded by the regional broadband seismic stations at epicentral distances up to 2500 km. The calculations were conducted over 27 stations in the Far East of the Russian Federation, in Japan, and Alaska (Fig. 4). The records were obtained from the collection of the IPC Petropavlovsk and IRIS DMC world database.

From the initial waveforms filtered in the period band $T = T_1 - T_2$, we selected the fragments of the records in the time window $[t_p, t_p + d]$ where t_p is the onset of the P -wave and d is the window's width. For the NIAE, $T = 100-400$ s and $d = 600$ s.

Based on the selected fragments, we estimated the following parameters: the depth h of the equivalent source, the duration τ of the source-time function (the duration of the slip in the source), and seismic moment tensor (SMT) for the double couple without a moment source model.

Table 3. Peak amplitudes of strong ground motion from NIAE of July 17, 2017, $M_W = 7.8$

No.	Station code	Δ , km	A_{peak} , cm/s ²			V_{peak} , cm/s		
			component			component		
			N	E	Z	N	E	Z
1	ADM	691	691	0.5	0.3	0.2	0.6	0.3
2	DAL	683	683	0.3	0.4	0.2	0.6	0.3
3	DCH	690	690	0.6	0.6	0.3	0.5	0.4
4	GPN	580	580	1.4	1.5	0.6	0.8	0.8
5	IVS	692	692	0.8	0.7	0.6	0.4	0.6
6	KBG	445	445	3.5	3.2	1.9	3.1	1.5
7	KLY	553	553	1.7	1.5	0.7	2.2	1.4
8	KOZ	603	603	2.2	2.1	0.8	2.8	2.4
9	KRM	730	730	1.0	0.9	0.6	0.5	0.3
10	KUR	1807	1807	0.1	0.1	0.1	0.1	0.1
11	NIC	709	709	0.7	1.0	0.3	0.5	0.4
12	NLC	641	641	1.2	1.0	0.4	0.7	0.3
13	NVA	2001	2001	0.1	0.1	0.0	0.2	0.1
14	OKH	1690	1690	0.2	0.1	0.1	0.3	0.3
15	OSS	651	651	0.2	0.2	0.2	0.2	0.4
16	PAL	757	757	0.1	0.2	0.1	0.2	0.3
17	PAU	870	870	0.2	0.2	0.1	0.3	0.2
18	PET	690	690	0.3	0.2	0.2	0.6	0.3
19	RIB	701	701	0.9	0.8	0.2	0.5	0.4
20	SCH	691	691	0.5	0.5	0.2	0.5	0.5
21	SHO	1971	1971	0.0	0.0	0.0	0.1	0.1
22	SK2	957	957	0.4	0.5	0.3	0.3	0.2
23	SKR	955	955	0.6	0.6	0.2	0.3	0.2
24	SPN	600	601	0.7	0.9	0.5	0.7	0.5
25	SPZ	688	688	0.6	0.5	0.2	0.6	0.3
26	TL1	698	698	0.4	0.5	0.3	0.5	0.6
27	TUMD	553	553	1.5	1.6	1.0	1.6	0.8
28	TYV	1802	1802	0.0	0.1	0.0	0.1	0.1
29	UGL1	1926	1926	0.1	0.1	0.1	0.2	0.1
30	UK1	453	453	3.5	4.4	1.7	4.2	2.2
31	UK2	448	448	3.2	2.7	1.5	4.0	1.6
32	UK4	455	455	4.5	4.6	1.9	3.7	2.5
33	VIL	709	709	1.1	0.7	0.3	0.5	0.4
34	VST	689	689	0.3	0.4	0.2	0.6	0.3

Δ is epicentral distance; A_{peak} is maximum amplitude of peak acceleration, V_{peak} is maximum amplitude of peak velocity.

The solution is found from the condition of the minimum residual ϵ , which reflects the misfit between the observed and synthetic seismograms (Pavlov and Abubakirov, 2012). The residual is calculated as the sum of the squared differences of the readings of the real and synthetic seismograms normalized to the sum

of the squared readings of the real seismograms, expressed in percentage. In Fig. 8a it can be seen that the residual changes insignificantly in the depth interval $h = 5\text{--}50$ km. This means that it is impossible to reliably determine the depth of the equivalent point source based on the results of waveform inversion at

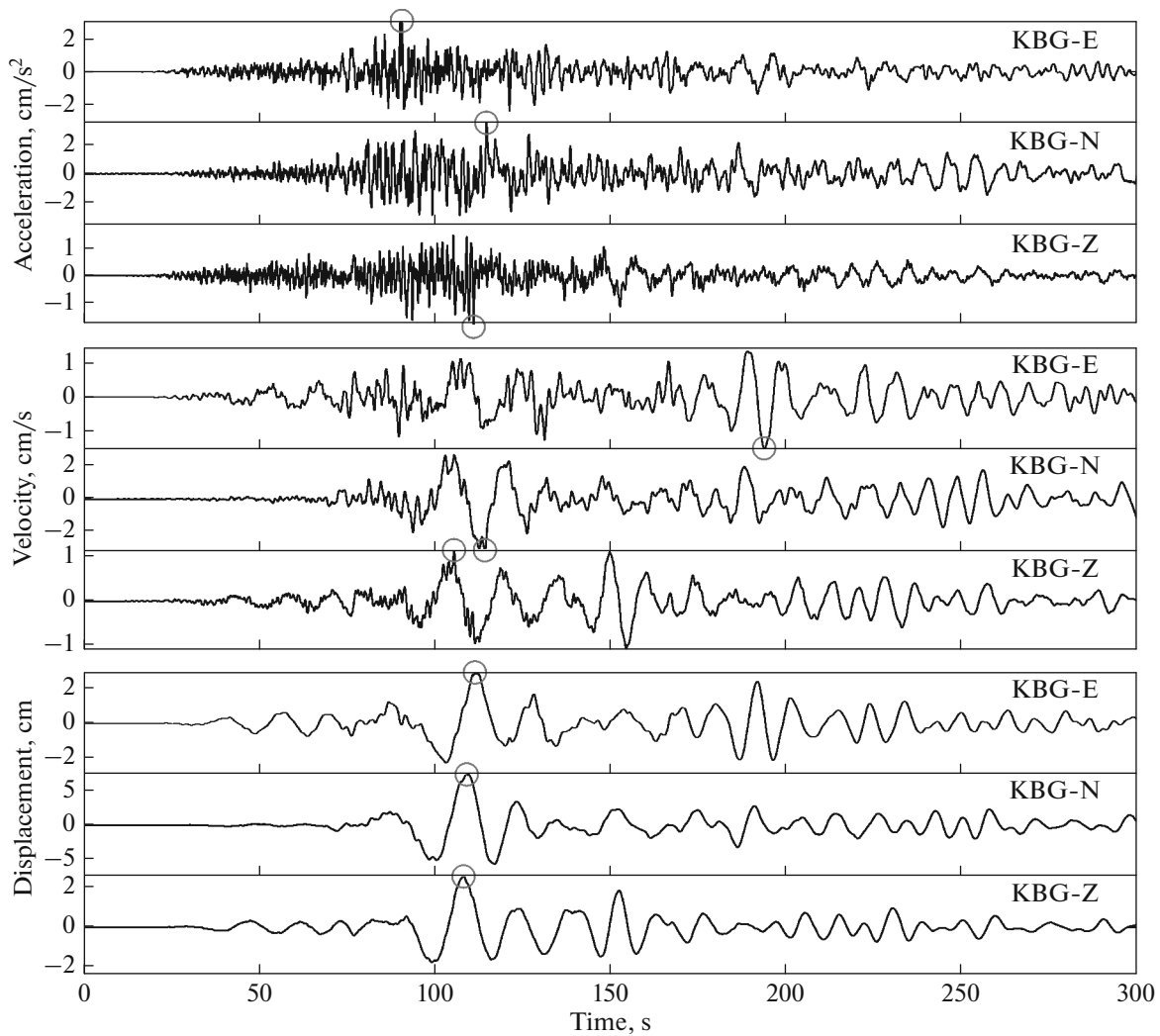


Fig. 6. Time behavior of acceleration, velocity, and ground displacement at KBG seismic station during NIAE according the CMG-DM24 accelerometer data ($\Delta = 478$ km, Fig. 4). Peak values are indicated by circle. Processing carried out in frequency band 0.02–20 Hz.

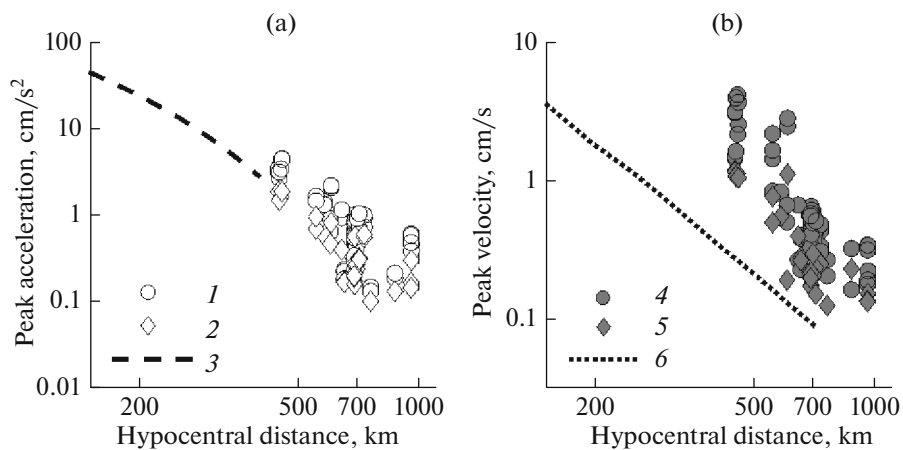


Fig. 7. Peak accelerations and velocities as functions of distance at NIAE: (a) acceleration dependence on hypocentral distance for horizontal (1) and vertical (2) components compared to typical dependence for Japanese Islands according to (Fukushima and Tanaka, 1992) for $M_W = 7.7$ (3); (b) velocity dependence on hypocentral distance for horizontal (4) and vertical (5) components and decay curve (6) obtained based on calibration curve of Fedotov energy class (Fedotov, 1972) for $K_{5.2}^{F68} = 16.1$.

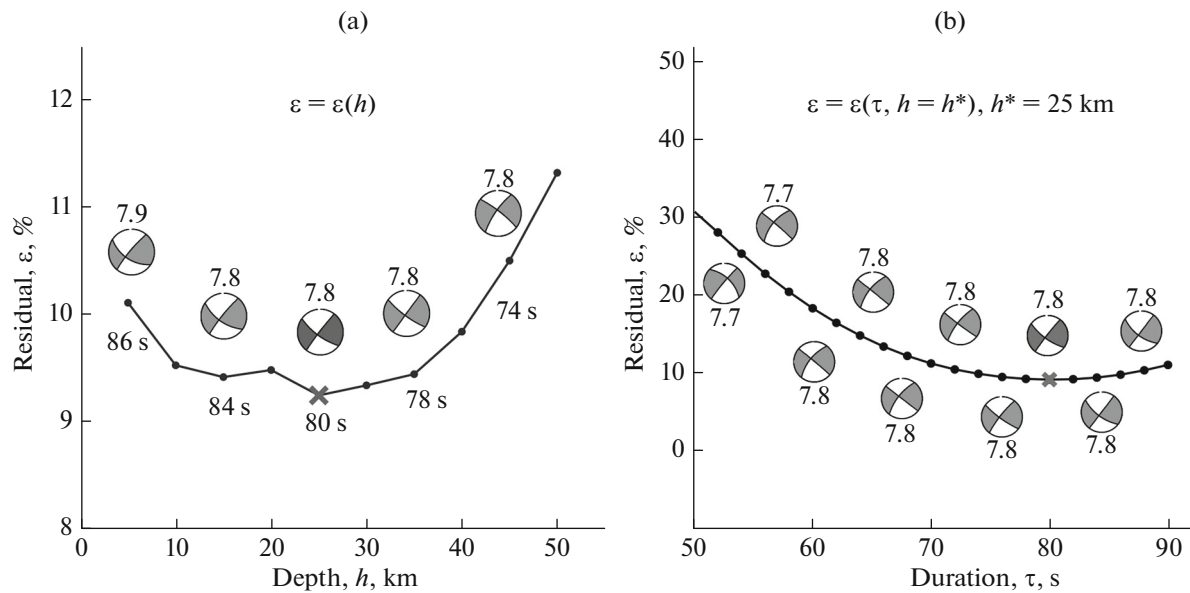


Fig. 8. Dependence of inconsistency measure between observed and synthetic seismograms (residuals ε) (a) on depth and (b) duration at fixed depth $h^* = 25$ km. Residual ε is calculated as sum of squared differences of data points in real and synthetic seismograms normalized to sum of squares of data points in real seismograms. Focal mechanisms in stereographic projection of lower hemisphere are shown. Numbers in stereograms are M_W values. Numbers near curve (a) are durations at given depth. Cross marks points corresponding to minimum residual.

regional distances. Therefore, as an estimate of the depth of the equivalent point source, we assume the interval $h = 5\text{--}50$ km.

The residual ε is sensitive to the slip duration τ . For the depth range $h = 5\text{--}50$ km, we determined the range of τ in which ε varies insignificantly: $\tau \approx 70\text{--}90$ s. The example of the dependence of ε on τ in Fig. 8b illustrates the sensitivity of the residual to the duration of the slip at a fixed depth h . In this example, the residual on interval $\tau \approx 70\text{--}90$ s is minimal and close to constant.

Based on SMT, we identified the focal mechanism of the NIAE and calculated the scalar seismic moment M_0 and moment magnitude M_W . The parameters of the principal axes of SMT and the estimates of scalar parameters of the equivalent point source h , τ , M_0 , and M_W are presented in Table 4, together with the independent estimates obtained at international centers. The stereograms of the mechanisms shown in Fig. 8 give an idea of the variability of the NIAE mechanism under waveform inversion at regional distances.

The focal mechanism parameters obtained by the independent information processing centers are close to each other. The fault planes are fairly steep, the slip type is either a right-lateral strike slip on the fault plane corresponding to the strike of the Bering Fault or a left-lateral strike-slip on the alternative plane cutting the island arc. Considering the strike of the NIAE aftershock cloud along the Bering Fault (Fig. 3), as the fault plane we select the *NPI* nodal plane (Table 4) with the northwest–southeast strike.

We note a significantly larger, compared to the data of the other information centers, rupture duration in the source ($\tau \approx 70\text{--}90$ s) calculated in KAGSR from the inversion of *long-period* waveforms. In the GCMT catalogs, the value is not calculated but specified according to the correlation dependence $\tau(M_W)$ (Ekstrom et al., 1992; 2012) and is 37 s, which is half the cited value. At the same time, in (Lay et al., 2017), based on the records of *short-period P*-waves, it is shown that the rupture in the NIAE source also occurred during $\sim 80\text{--}100$ s. Thus, our estimate $\tau \approx 70\text{--}90$ s is supported by the calculations from the independent data.

ANALYSIS OF COSEISMIC DISPLACEMENTS AND ESTIMATING THE SOURCE MODELS FROM GNSS DATA

The coseismic displacements from the NIAE are detected by most of the GNSS stations installed on the Kamchatka Peninsula, Commander Islands, and Aleutian Islands closest to the epicenter (Fig. 9).

The coseismic displacements were determined from the time series of station coordinates obtained by processing the GNSS observations in the static mode by the GAMIT/GLOBK software package (Herring et al., 2010). A network of 51 stations was processed, including the Kamchatka GNSS network, the closest IGS stations, and five stations of the Plate Boundary Observatory (PBO) network on the Aleutian Islands. For reducing the time series variance, the processing was conducted in the conditional reference frame

Table 4. Summary of focal mechanism parameters for NIAE of July 17, 2017

SMT parameters													
Data center	SMT principal axes ¹						Nodal planes ²						Focal mechanism beach-ball plot ³
	<i>T</i>		<i>N</i>		<i>P</i>		<i>NP1</i>			<i>NP2</i>			
	<i>azm</i>	<i>pl</i>	<i>azm</i>	<i>pl</i>	<i>azm</i>	<i>pl</i>	<i>stk</i>	<i>dip</i>	<i>slip</i>	<i>stk</i>	<i>dip</i>	<i>slip</i>	
KAGSR	84	16	229	71	351	10	126	71	175	218	86	19	
GCMT	262	2	13	85	172	5	307	85	-178	217	88	-5	
NEIC	260	15	113	72	352	9	305	86	163	37	73	4	
Scalar parameters of equivalent point source													
Data center	Depth <i>h</i> , km		Slip duration in source τ , s		Scalar seismic moment M_0 , N m		Moment magnitude M_W						
KAGSR	5–50		70–90		6.6×10^{20}		7.8						
GCMT	23		37		5.4×10^{20}		7.8						
NEIC	30		43		5.168×10^{20}		7.7						

¹ SMT principal axes: *T*, tension axis; *P*, pressure axis, *N*, intermediate axis. Axis orientation is specified by two angles: azimuth *azm* and plunge *pl*. ² Orientation of nodal planes *NP1*, *NP2* is specified by two angles: strike azimuth *stk* and dip angle *dip*. Slip angle *slip* is angle in fault plane between strike direction and displacement vector (measured counterclockwise from strike direction). Angles are in degrees. ³ In equal-area projection of lower hemisphere.

h is depth of equivalent point source, τ is slip duration in source, M_0 is scalar seismic moment, M_W is moment magnitude.

fixed to the IGS sites unaffected by the earthquake with the zero initial a priori velocities. The coseismic displacements for the nearest BRNG and AC60 stations were estimated as the difference of the regression lines determined from ten observations (readings) (ten days) before the earthquake and the first observation after the earthquake. For the other stations, the coseismic displacements were determined as the difference of the 10-day regression lines before and after the earthquake. The results of estimating the coseismic displacements are presented in Table 5.

The largest displacements are identified at the GNSS stations that are closest to the epicenter: the BRNG station ($\Delta \sim 200$ km, no. 3 in Fig. 9 and in Table 5) on the Bering Island and AC60 station ($\Delta \sim 600$ km, no. 2 in Fig. 9 and in Table 5) on the Simiya Island. During the first day after the earthquake, the BRNG station moved 72 mm west-southwestwards. This jump exceeds the characteristic annual displacement of the Commander microplate (~ 55 mm/yr relative to Eurasia (Levin et al., 2012)) and occurs in a different direction than this displacement.

After the event, a postseismic displacement is detected at the BRNG station, which testifies to the continuing active phase of the geodynamic process initiated by NIAE. As of February 24, 2018, the horizontal components of this displacement were -49 mm eastwards and -8 mm northwards. Thus, the postseis-

mic displacement occurs practically in the same direction as the coseismic jump and, as of the date of writing this paper, measures $\sim 70\%$ of the latter.

For estimating the parameters of the extended source, we modeled the coseismic displacements. The calculations were conducted with a model of an extended dislocation source in a homogeneous elastic isotropic half-space (Okada, 1985). At the first stage, we compared the recorded horizontal displacements with the displacements predicted by the NEIC Finite Fault¹⁰ multicomponent source model consisting of 400 rectangular finite dislocations with the slip parameters calculated by the inversion of the waveform data. The total size of the rupture area is $\sim 375 \times 60$ km², the slips on separate segments range from 0 to 3 m. Based on these data, we calculated the model surface displacements using the Coulomb34 program package (Toda et al., 2011). These calculations have shown that the NEIC Finite Fault model is poorly consistent with the GNSS data (Table 5). The observed displacements are overall 1.3 times the size of the model ones; moreover, at the BRNG and AC60 stations, which are closest to the epicenters, the observed values are 2.4 and 1.6 times greater than the model predictions, respectively.

¹⁰ <https://earthquake.usgs.gov/earthquakes/eventpage/us20009x42#finite-fault>

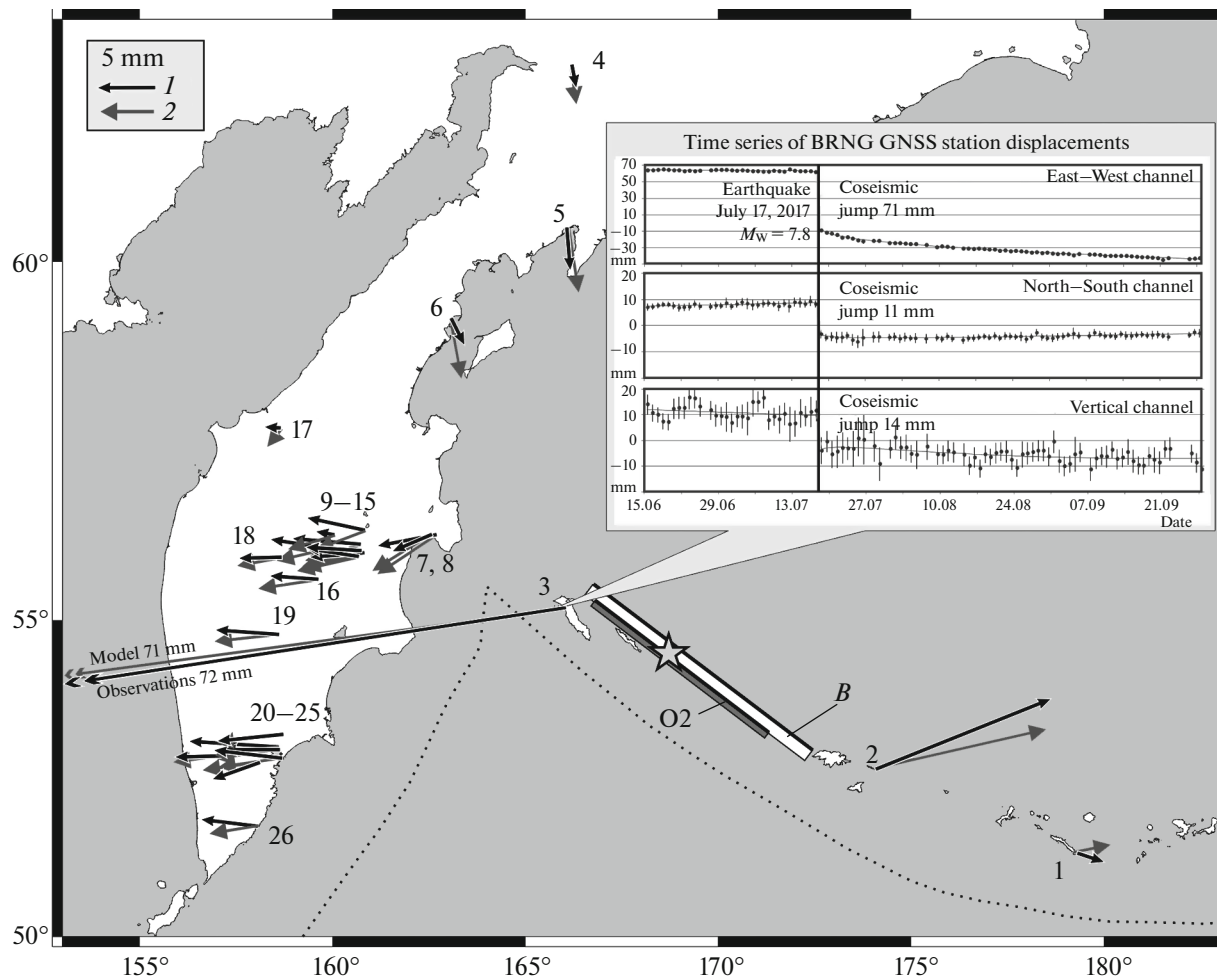


Fig. 9. Horizontal coseismic displacements caused by NIAE. Black and gray arrows correspond to observation results and optimal O2 model, respectively. Dotted line is Pacific Plate boundary. Rectangle O2 is projection of O2 model source; rectangle B is surface projection of model source area from (Lay et al., 2017) (bilateral slip). Asterisk marks NIAE epicenter. Inset shows time series of BRNG GNSS station displacements (no. 3 in Fig. 9 and Table 5). BRNG site displacement is shown out of scale.

As the next step, we estimated the parameters of a simple model of a rectangular dislocation source uniform along the slip, which reasonably adequately describes the real displacements. At most stations, the recorded displacements are close to the accuracy limit of the GNSS measurements. Therefore, for constructing the source model, we initially used only the data from two stations, BRNG and AC60, closest to the epicenter, at which the recorded coseismic displacements are maximal. Subsequently, based on the obtained model parameters, we calculated the residuals for the entire network of the stations.

We considered two models, O1 and O2 (Table 5), with the fault planes dipping northeast and southwest, respectively. The strike azimuth, dip angle, and the mean slip angle for the O1 model correspond to the NEIC Finite Fault model. The same parameters for the O2 model correspond to the orientation and slip angle of the *NPI* nodal plane of the NIAE focal mechanism calculated at KB GS RAS (Table 4, KAGSR).

The sought parameters comprise the coordinates of the center, the width, and the length of the source area. The search was conducted with a step of 1 km across the coordinates of the center along the strike azimuth within 100 km on either side of the KAGSR epicenter (Table 1); across values of the width and length within 10–80 and 50–500 km, respectively. The other source parameters are fixed during the search. The scalar seismic moment was specified in accordance with the NEIC Final Fault model and assumed to be $M_0 = 6.67 \times 10^{20}$ N m. The slip was calculated from the relation

$$\text{Slip} = M_0 / (S\mu),$$

where S is the source area in m^2 and $\mu = 4.44 \times 10^{10}$ N/m² is the shear modulus (the average spherical model ak135f¹¹). The area providing the minimum residual

¹¹ <http://rses.anu.edu.au/seismology/ak135/ak135f.html>

Table 5. Recorded and model coseismic displacements from NIAE according to GNSS observations

No.	GNSS site	Longitude, φ	Latitude, λ	Observed displacements \pm error, mm			Model displacements, mm											
				E	N	U	NEIC Finite Fault model			model O1			model O2			model C		
							E	N	U	E	N	U	E	N	U	E	N	U
1	AC66	179.30	51.38	2.4 \pm 1.8	0.8 \pm 1.7	0.4 \pm 4.5	8.9	1.9	-0.8	3.3	0.5	-1.1	3.2	0.6	-1.1	3.6	0.3	-1.3
2	AC60	174.08	52.72	15.0 \pm 2.2	3.6 \pm 1.1	-9.4 \pm 3.3	1.9	0.5	-0.4	15.0	3.0	-4.1	15.0	3.4	-4.7	17.6	1.7	-5.7
3	BRNG	165.98	55.19	-71.1 \pm 1.1	-11 \pm 1.8	-14 \pm 5	-29.8	-3.7	-2.8	-70.9	-9.8	-17.9	-70.7	-9.5	-9.2	-71.1	-13.2	-7.2
4	KMS1	166.21	62.47	0.4 \pm 1.5	-2.1 \pm 1.6	0.4 \pm 5.7	0.3	-2.3	0.7	0.4	-3.4	1.2	0.4	-3.2	1.2	0.3	-2.7	1.0
5	TILI	166.15	60.45	0.3 \pm 1.3	-3.8 \pm 1.1	-2.1 \pm 4.7	0.7	-4.0	1.2	0.8	-5.8	2.0	0.8	-5.5	2.0	0.5	-4.3	1.6
6	OSSS	163.07	59.26	1.2 \pm 1.6	-2.4 \pm 2.0	1.9 \pm 7.7	0.5	-3.0	0.7	0.8	-5.2	1.7	0.9	-5.1	1.7	0.3	-3.5	1.1
7	_KBG	162.71	56.26	-5.2 \pm 0.8	-1.0 \pm 1.1	-1.0 \pm 4.4	-4.3	-1.3	-1.0	-5.9	-2.9	-1.5	-5.1	-3.3	-0.9	-5.1	-1.6	-1.3
8	UKAM	162.59	56.27	-3.5 \pm 1.5	-1.5 \pm 1.2	0.2 \pm 3.3	-4.3	-1.2	-1.0	-5.8	-2.7	-1.5	-5.0	-3.2	-0.9	-5.0	-1.5	-1.3
9	KLU1	160.86	56.32	-5.1 \pm 0.9	1.1 \pm 0.8	3.6 \pm 3.7	-3.5	-0.6	-0.9	-4.6	-1.4	-1.4	-4.2	-1.6	-1.1	-3.9	-0.7	-1.2
10	APH1	160.84	56.00	-4.8 \pm 0.8	-0.4 \pm 1.0	-2.1 \pm 6.0	-4.2	-0.5	-1.1	-5.6	-1.1	-1.9	-5.3	-1.3	-1.6	-4.6	-0.6	-1.5
11	PIR1	160.77	56.03	-4.9 \pm 1.2	0.3 \pm 1.2	0.2 \pm 6.7	-4.0	-0.5	-1.1	-5.5	-1.1	-1.8	-5.1	-1.3	-1.5	-4.5	-0.6	-1.5
12	CIR1	160.75	56.12	-6.0 \pm 1.4	0.5 \pm 1.4	0.1 \pm 6.4	-3.8	-0.5	-1.0	-5.2	-1.1	-1.7	-4.8	-1.3	-1.4	-4.3	-0.6	-1.4
13	BZGD	160.70	55.94	-4.6 \pm 0.6	0.7 \pm 2.3	-0.7 \pm 3.7	-4.2	-0.5	-1.2	-5.6	-1.0	-1.9	-5.4	-1.2	-1.6	-4.7	-0.5	-1.5
14	MAYS	160.06	56.25	-1.7 \pm 1.6	0.3 \pm 1.3	-3.1 \pm 7.0	-3.3	-0.4	-0.9	-4.3	-1.0	-1.4	-4.0	-1.2	-1.1	-3.6	-0.5	-1.2
15	KOZS	159.87	56.06	-5.0 \pm 1.4	0.8 \pm 1.7	-2.3 \pm 5.0	-3.5	-0.4	-1.0	-4.6	-0.8	-1.6	-4.4	-1.0	-1.3	-3.9	-0.4	-1.3
16	ATLS	159.65	55.61	-4.3 \pm 1.5	0.3 \pm 1.5	0.1 \pm 4.1	-3.9	-0.3	-1.2	-5.4	-0.6	-1.9	-5.2	-0.7	-1.7	-4.4	-0.3	-1.5
17	TIGS	158.67	57.77	-1.5 \pm 1.1	0.1 \pm 1.1	1.7 \pm 4.0	-1.3	-0.6	-0.3	-1.4	-1.4	-0.2	-1.2	-1.5	-0.0	-1.4	-0.9	-0.3
18	_ES1	158.70	55.93	-3.8 \pm 1.3	-0.1 \pm 1.1	-0.3 \pm 4.1	-3.0	-0.3	-0.9	-4.0	-0.6	-1.4	-3.9	-0.7	-1.3	-3.4	-0.3	-1.2
19	MIL1	158.58	54.68	-5.6 \pm 0.9	0.4 \pm 1.4	0.9 \pm 4.4	-3.9	-0.4	-1.2	-5.3	-0.5	-2.0	-5.4	-0.5	-1.9	-4.4	-0.2	-1.6
20	AVCH	158.74	53.26	-5.8 \pm 1.2	-0.6 \pm 0.9	3.4 \pm 6.7	-4.0	-0.6	-1.3	-5.5	-0.6	-2.1	-5.8	-0.8	-2.2	-4.7	-0.4	-1.8
21	MYAK	158.71	52.89	-6.0 \pm 1.2	0.7 \pm 2.1	-2.2 \pm 8.5	-3.8	-0.6	-1.2	-5.3	-0.7	-2.0	-5.6	-0.8	-2.1	-4.5	-0.4	-1.7
22	PETS	158.65	53.02	-5.0 \pm 1.3	-0.0 \pm 1.1	-0.9 \pm 7.0	-3.8	-0.6	-1.2	-5.3	-0.6	-2.0	-5.6	-0.8	-2.1	-4.5	-0.4	-1.7
23	PETR	158.61	53.07	-7.8 \pm 1.0	0.5 \pm 1.4	-7.1 \pm 5.6	-3.8	-0.6	-1.2	-5.3	-0.6	-2.0	-5.6	-0.7	-2.1	-4.5	-0.4	-1.7
24	KMSH	158.13	52.83	-4.2 \pm 0.9	-1.5 \pm 1.4	-1.1 \pm 5.2	-3.4	-0.5	-1.1	-4.7	-0.6	-1.8	-5.0	-0.7	-1.9	-4.0	-0.4	-1.5
25	APC1	157.13	52.93	-4.1 \pm 0.9	-0.1 \pm 1.7	1.0 \pm 6.6	-3.1	-0.4	-1.0	-4.1	-0.5	-1.6	-4.3	-0.5	-1.6	-3.5	-0.3	-1.3
26	VODO	158.08	51.81	-5.0 \pm 1.0	0.6 \pm 1.0	-1.2 \pm 4.5	-2.8	-0.5	-0.9	-4.0	-0.5	-1.5	-4.2	-0.7	-1.6	-3.4	-0.4	-1.3

Table 6. Parameters and residuals of models of extended dislocation sources for NIAE of July 17, 2017, $M_W = 7.8$

Model	Coordinates of center of source area ¹ , lat., °N; long., °E; depth, km	Width, km	Length, km	Orientation of source plane and slip ² , ° <i>strike</i> <i>dip</i> <i>rake</i>	Slip, m	Model residual ³ , mm	
						for BRNG and AC60 stations	for all stations
NEIC Finite Fault	54.19 ¹ 169.66 32.0	61.6	375	307 72 170 ± 30 ²	~0–2.99 ²	21.15	3.20
B (Lay et al., 2017)	54.49 ¹ 168.96 12.5	33	468	126 77 –173 ± 45 ²	~0–8.5 ²	–	–
O1	54.30 169.23 10.0	19	347	307 72 174	2.28	0.85	1.58
O2	54.17 169.11 10.5	20	354	126 71 175	2.12	0.82	1.61
Composite source C = CI + CII							
CI	53.90 169.90 10.5	20	200	130 71 175	3.04		
CII	55.30 166.89 10.5	20	50	126 71 175	1.00	2.71	1.39

¹ Coordinates of center, width and length are indicated for total source area. ² Strike azimuth (*strike*) and dip angle (*dip*) are constant for each element; slip and its angle (*rake*) vary on elements within indicated ranges. ³ Only horizontal components are taken into account.

for the BRNG and AC60 stations was accepted as the solution. The residual was calculated by the formula

$$\text{Residual} = \sum |Vm_i - Vo_i|/n,$$

where Vm_i is the vector of the model horizontal station displacement; Vo_i is the observed vector of the horizontal station displacement; n is the number of stations; and $|\dots|$ is the vector length.

The established values of the sought parameters of models O1 and O2 are presented in Table 6. The values of the residuals and model displacements presented in Table 5 show that, based on the considered GNSS observations, it is impossible to decide between these two models. The detected displacements and the ones calculated for the O2 model are shown in Fig. 9.

The rupture area is estimated at $\sim 350 \times 20 \text{ km}^2$ which is, in terms of the length, two thirds the extent of the NIAE aftershock cloud. The center of the rupture is shifted by $\sim 23 \text{ km}$ southeast relative to the NIAE epicenter (Table 6, Fig. 9). The slip in the source is 2.1–2.3 m.

From Fig. 9 it can be seen that even this simple model yields a reasonably close agreement between the horizontal vectors of the model and real displacements. A somewhat better agreement for the same GNSS data was achieved by the authors of (Lay et al., 2017)¹² who considered a complex spatiotemporal source model initially based on the inversion of the recorded seismic waves. In their model, the source is also located in the vicinity of the Bering Fault; however, in contrast to the two previous models, the slip is not assumed to be uniformly distributed on the fault rupture. According to the obtained estimates, the maximum slip is observed about 100 km (from 50 to 200 km) southeast of the epicenter and, separately, close to the northwestern termination of the rupture.

A number of independent observations also suggest that the NIAE source should probably be considered as a composition of two almost simultaneous events. During the first hours after the main shock, in the

¹²Lay et al. (2017) also used the GNSS data from the BRNG station pertaining to the KB GS RAS GNSS network.

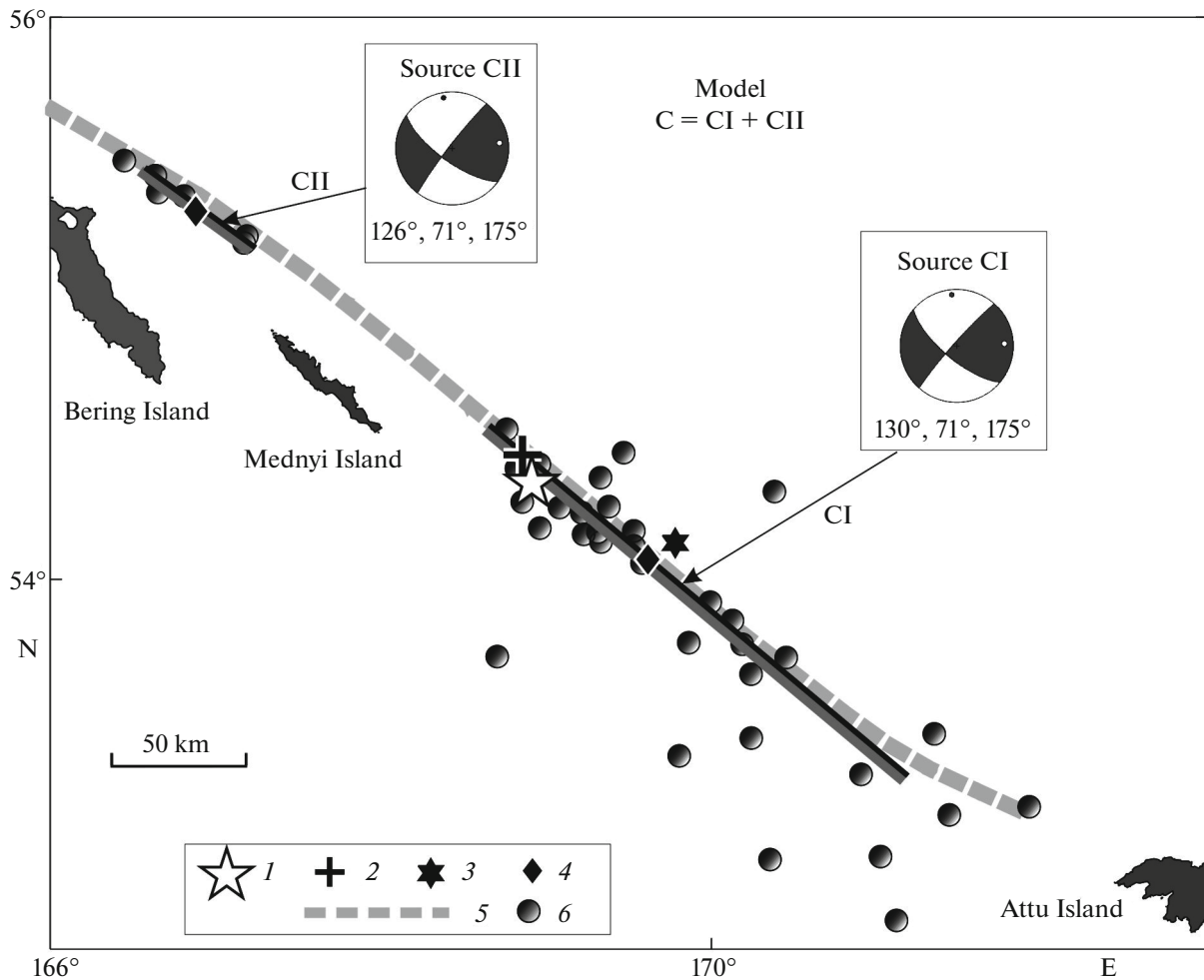


Fig. 10. Combined source C consisting of two dislocation sources CI and CII. Projections of upper edges of CI and CII source areas are shown (parameters presented in Table 5). 1, KAGSR epicenter; 2, NEIC epicenter; 3, GCMT centroid; 4, geometrical centers of projections; 5, Bering Fault; 6, first-three-hour aftershocks according to NEIC catalog. Mechanisms are shown for CI and CII.

central part of the fault spanning more than 100 km a segment existed northwest of the epicenter where the aftershocks were not detected (Figs. 10, 12b). Judging by the fact that at the end of the first day, the aftershocks began to occur also in this area, here we are dealing with a segment whose activation was delayed rather than with a segment where the stresses were released during the main shock.

Considering this and taking into account the estimates of (Lay et al., 2017), we additionally analyzed the NIAE model C, which is composed of two sub-sources CI and CII and estimated their probable seismic moments and magnitudes. The segments of the maximum slip obtained in (Lay et al., 2017) practically coincide with the areas of the early aftershocks. Therefore, the positions of the sub-sources in model C are fixed a priori based on the size of the separated cloud of the first three-hour aftershocks (Figs. 10, 12b).

Model C consists of two subparallel sources CI and CII located along the Bering Fault at a distance of ~100 km from each other and slightly different from each other in orientation following the varying trend of the fault (Fig. 10, Table 6). The southeastern CI source is the main one; it has a length of 200 km, a width of 20 km, fault plane orientation with a *strike* of 130° and *dip* of 71°, and slip orientation with a *rake* of 175°. The northwestern CII source is secondary. Its length is 50 km, the width is 20 km, the fault plane and slip orientation is (*strike* 126°, *dip* 71°, *rake* 175°).

Note that for both sub-sources, the *dip* and *rake* parameters are assumed in accordance with the KAGSR focal mechanism solution (Table 4, *NP1* plane). The positions of the centers of the sources are specified by the geographical coordinates presented in Table 6. The unknown estimated model parameters are *UI* and *UII*—the slip lengths in CI and CII, respectively.

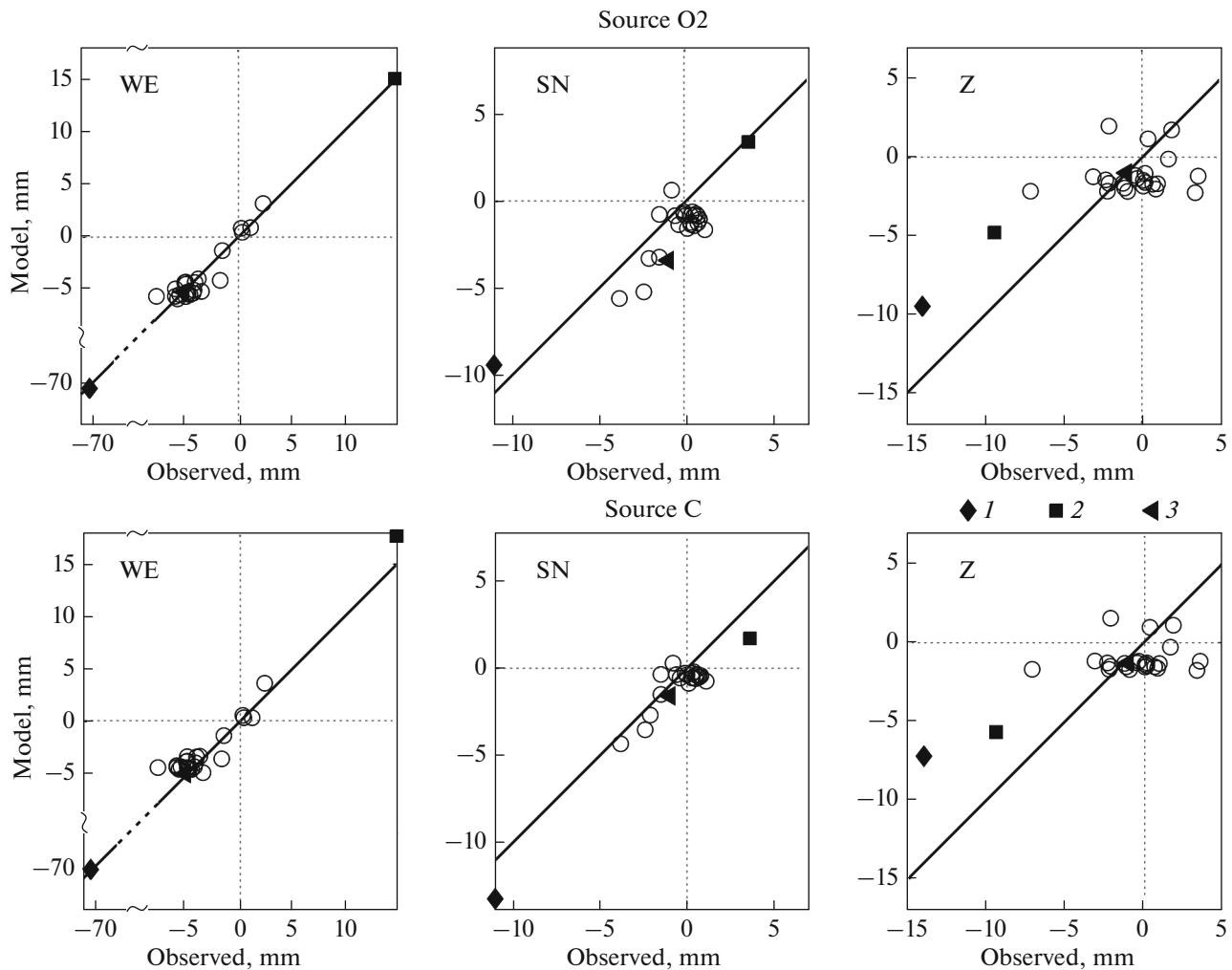


Fig. 11. Comparison of model and observed components of coseismic displacements for model O2 (top) and combined model C (bottom). Displacement values at three stations closest to NIAE epicenter are shown by markers 1 (BRNG station on Bering Island), 2 (AC60 at Simiya Island), and 3 (KBG on Kamchatka Peninsula) (nos. 3, 2, and 7 in Fig. 9 and Table 5). Oblique line is geometric locus of points of perfect fit between model and observed displacements.

In this case, in the inversion we used the values of three displacement components (including the vertical component) measured by all the GNSS stations presented in Table 5. The unknown parameters were estimated by the method from (Levin et al., 2010).

The results of the inversion are presented in Table 6, and the comparison of the observed and model displacement components is illustrated in Fig. 11. We note that since the inversion was carried out with the data from all the GNSS stations and all components, the resulting residuals for the two stations closest to the epicenter in model C are slightly larger than the respective values for model O2 but are still quite reasonable.

The obtained estimates of the slip lengths UI and UII are 3.04 and 1.00 m, which is consistent with the estimates of the seismic moments and moment magni-

tudes: for CI $M_0 = 5.4 \times 10^{20}$ N m and $M_W = 7.8$; and for CII, $M_0 = 4.4 \times 10^{19}$ N m and $M_W = 7.0$.

Thus, model C composed of two separate sources is consistent with the observations of coseismic displacements.

MAIN RESULTS AND DISCUSSION

The Near-Island Aleutian earthquake (NIAE) with magnitude $M_W = 7.8$ that occurred on July 17, 2017 at 23:34 UT (July 18, 2017 at 11:34 LT) is one of the strongest instrumentally recorded seismic events in the western part of the Aleutian island arc. The earthquake's hypocenter is located near the eastern edge of the Commander Islands shelf on the back-arc Bering transform fault at a depth of up to ~ 25 km. The cloud of the foreshocks and aftershocks stretch over ~ 500 km along the strike of the arc. The foreshock activity

appeared approximately 11 months before the main shock, whereas the decaying aftershock sequence lasted about 3.5 months after the main shock. Subsequently, noticeable non-stationary activity exceeding the background level was observed in the source area. As of the beginning of March 2018, this activity had not yet died out.

The prompt estimates (according to the TWC regulations, the processing time is at most 10 min) suggest that the instrumental hypocenter of the NIAE was located at a shallow depth ~ 6 km beneath the seafloor of the Bering Sea and the magnitude of the earthquake was M_S (PET) = 7.6. According to the magnitude–geographical criterion based on these parameters, the NIAE corresponded to a potentially tsunamigenic earthquake, and the tsunami alert was issued accordingly. However, a small tsunami perturbation with a height of ~ 0.1 m was instrumentally detected only in the region of the Near Islands of the Aleutian Ridge.

The final analysis of the NIAE data was based on the records from 55 seismic stations and 51 GNSS stations, most of which pertain to the Kamchatka system of the KAGSR seismological and geophysical monitoring; the remaining stations are located in the adjacent regions. Numerous oral interviews and written inquiries among local people were conducted.

According to the information of the macroseismic data service at KB FRC GS RAS, the ground shaking intensity I at the closest Nikol'skoe locality on Bering Island (~ 200 km northwest of the NIAE epicenter) reached 5–6 on the MSK64 scale. On the Kamchatka Peninsula, the NIAE was felt with intensity I up to 3–4.

The preliminary analysis of the NIAE ground motion data is carried out. The estimates of the maximal velocities and accelerations are obtained for 34 seismic stations at the epicentral distances ranging from ~ 450 to ~ 2000 km. The level of peak ground acceleration amplitudes at distances up to 800 km proved to be comparable with the respective parameters for the typical earthquakes of Japan. At the same time, the measured values of the decay parameters and the level of peak velocities markedly differ from the ones expected from the energy class calibration curves which are used in the current processing of the Kamchatka data. This is due to the significant difference in the operating frequency bands of the modern broadband digital loggers and the analog instruments whose records were used for constructing the calibration curve.

Based on the NIAE records by 27 broadband seismic stations located in the Far East of the Russian Federation, Japan, and Alaska, the estimates are calculated of the seismic moment tensor, the depth of the equivalent point source (5–50 km), and slip duration in the source (70–90 s). The obtained focal mechanism is close to the results determined by the other data centers. This mechanism supports the predominance of the right-lateral strike-slip displacements in the northeastern boundary of the Commander block

(on the subvertical Bering Fault) reflecting the rapid sliding of this block relative to the Beringia lithospheric plate.

The model of dislocation in the NIAE source which uses the constructed focal mechanism also allows the description of the measured coseismic GNSS station displacements with the simultaneous estimation of the size and position of the source on the Bering Fault. The GNSS data processing included the records from many stations; however, at most stations, the recorded displacements are close to the limit of the measurement accuracy. Therefore, for determining the model of the source, we primarily used the data from the two closest stations at which the coseismic displacements are maximal: the BRNG and AC60 stations with horizontal displacements of 72 and 15 mm, respectively. The reasonably close consistency with the GNSS data was achieved with the simplest model of a rectangular source with a uniform slip. Moreover, the model also fairly well described the slip at the remote stations of the Kamchatka region. The rupture area is estimated at $\sim 350 \times 20$ km and the slip in the source at ~ 2.1 – 2.3 m.

Nevertheless, a number of other facts and the estimates obtained for the NIAE are not well described by the model of a single source. The length of the rupture predicted by this model is ~ 350 km, which is approximately two-thirds the length of the cloud of NIAE aftershocks. However, this estimate is larger than the typical source size of the strike-slip earthquakes with magnitudes 7.7–7.8. According to the empirical dependences (Wells and Coppersmith, 1994; Papazachos et al., 2004; Thingbaijam et al., 2017), the average expected length of the ripped rupture for $M_w = 7.8$ is 180–240 km (considering the scatter, 130–330 km). During the first hours after the main shock, in the forming cloud of the aftershocks, there is an extended (longer than 100 km) gap (Fig. 12b) probably reflecting the substantial nonuniformity of the distribution of the main slip along the Bering Fault. The same is also suggested by the results of the inversion of the source parameters carried out in (Lay et al., 2017).

These shortcomings of the simplest model can be eliminated if we assume that the main event contained two subsources which are close in time but spatially separated along the Bering Fault: one covering 200×20 km in the southeast and another covering 50×20 km in the northwest (Fig. 10, model C in Table 6). These sizes of subsources are selected in accordance with the shape of two separate clouds of aftershocks that emerged during the first hours after the main shock (Fig. 12b) and later merged. Within this model, the NIAE scenarios could be described in the following way:

—the earthquake occurred on the Bering Fault and the main slip CI was accommodated by the southeastern part of the fault, which had been relatively inactive during the previous decades (Fig. 12a);

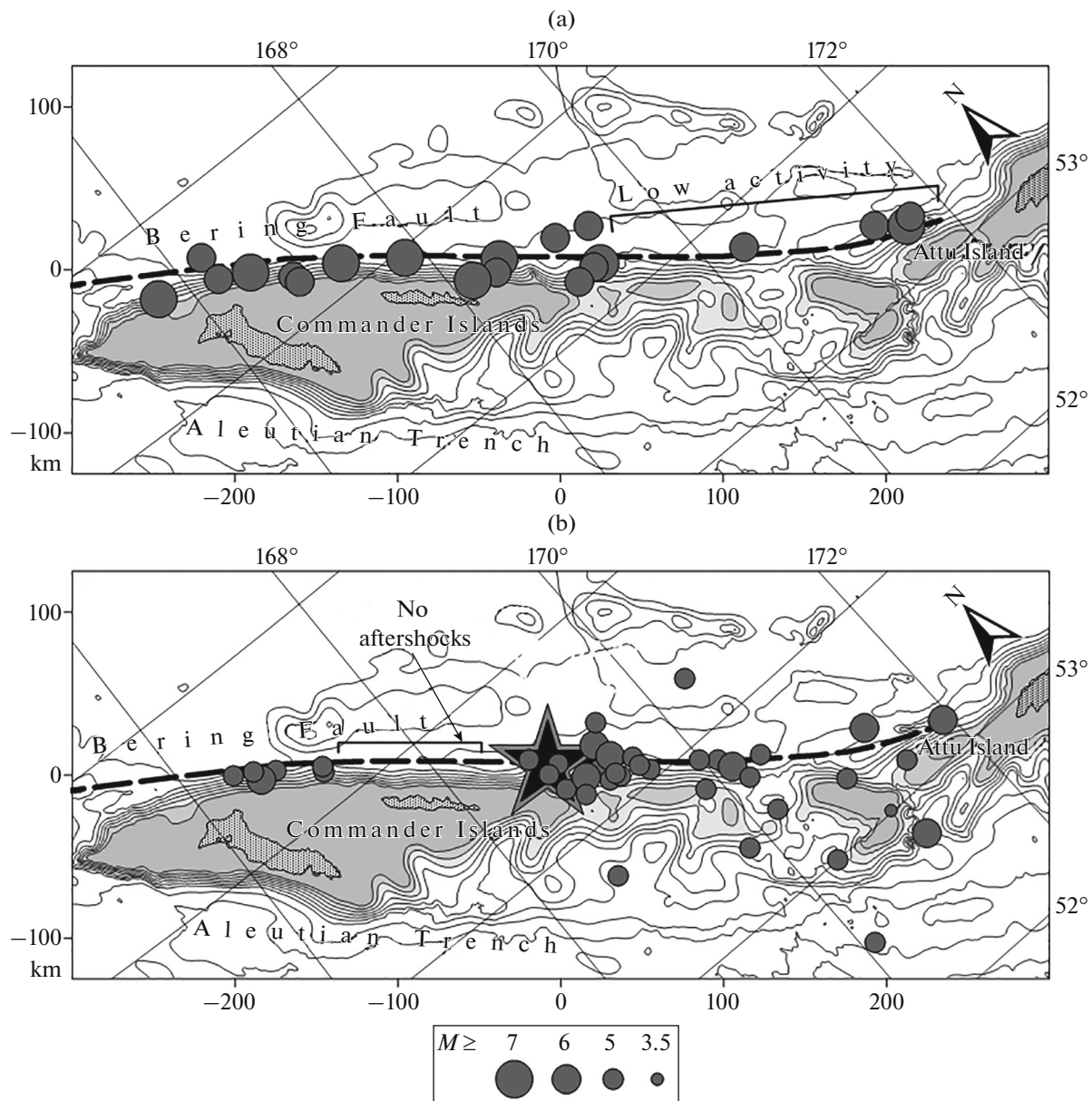


Fig. 12. Seismicity on Bering Fault: (a) strongest earthquakes with $M_W \geq 5.5$ with epicenters in vicinity of fault over 1962–2014 according to ISC–GEM catalog; (b) NIAE aftershocks recorded within three hours after main shock. Event coordinates are presented according to NEIC catalog. Asterisk is NIAE epicenter. Dashed line is Bering transform fault.

—since the earthquake’s epicenter (the origin of the process) is located at the northwestern termination of the CI segment, fracture propagation is likely to have developed from this segment towards the southeast;

—almost simultaneously, a smaller slip with a close focal mechanism occurred 100–200 km northwest of the main epicenter (opposite Bering Island), which provided the main contribution in the BRNG station displacement and, probably, in the displacement of the whole island;

—during the first few hours, the segment separating the two assumed subsources could remain passive

(Fig. 12b); however, toward the end of the first day, this segment was also involved in the common aftershock activity, which combined both subsources;

—the magnitude estimates constructed for each subsurface in the C model based on the GNSS data are $M_W = 7.8$ for the main southeastern subsurface and $M_W = 7.0$ for the smaller northwestern subsurface; thus, the northwestern event was significantly weaker than the southeastern one;

—the rupture duration estimates at 70–90 s obtained by (Lay et al., 2017) and by us should probably be attributed to the main southeastern subsurface.

The combination of the length (~200 km) and the rupture's duration yields the estimate of the rupture front's propagation velocity at ~2.5 km/s. This estimate is clearly lower than the shear wave velocity (3.9 km/s for the surface layer in the AK135f model). The Mach number is ~0.6;

—the identification of the southeastern subsource as the main one, *inter alia*, removes the contradiction between the excessively large length of the entire source and the typical size of the earthquakes with $M \sim 7.8$; the length of the CI segment ~200 km closely agrees with the empirical dependences of this parameter on magnitude; the same also applies for the smaller CII subsource whose length ~50 km is consistent with the magnitude obtained for it, $M_W = 7.0$.

The emergence of the NIAE provides additional evidence of the higher instrumental seismicity of the Commander microplate's northeastern boundary compared to the southwestern boundary. The southwestern boundary remains relative quiescent—the Commander seismic gap. The NIAE source has not filled the gap, and after this major event the contrast between the seismic activity on the Beringian and Pacific boundaries of the Commander block has become even more prominent. The structural and kinematic analogy of the Burma and Commander microplates, as well as the similarity of the observed scenario of seismicity with the events that preceded the Sumatran mega-earthquake of December 26, 2004, indicates that the northwestern part of the Aleutian Arc remains prone to a strong earthquake. The tsunami hazard from an earthquake in the region of the Commander gap is discussed in detail in (Lobkovsky et al., 2014; Mazova et al., 2013). We note that under a reverse fault—thrust displacement, which may occur if the Commander gap is activated, a potential earthquake with $M_W \geq 7.5$ will highly probably be tsunamigenic. In this situation, the Commander region requires greater attention.

FUNDING

The work was carried out as part of a state contract of KB GS RAS under project nos. AAAA-A16-116070550063-8 “Development of methods for assessing the tsunamigenic potential of strong earthquakes based on the analysis of their source parameters and wave fields for the tsunami warning system,” AAAA-A16-116070550059-1 “Complex study of earthquake precursors and development of methods for forecasting seismic setting in earthquake-prone regions,” and AAAA-A16-116070550057-7 “Conducting continuous seismic, geophysical, and geodynamic monitoring on global, federal, and regional levels: the development and implementation of new technologies for processing and systems analysis of large amounts of data” with the partial support from the Ministry of Science and Education of the Russian Federation

under project no. 14.W03.31.0033 “Geophysical study, monitoring, and forecasting the development of catastrophic geodynamic processes in the Far East of the Russian Federation,” and from the Russian Foundation for Basic Research under project no. 17-05-00185.

REFERENCES

- Abubakirov, I.R., Pavlov, V.M., and Titkov, N.N., The Mechanism of the deep-focus, Sea of Okhotsk earthquake of May 24, 2013 as inferred from static displacements and broadband seismograms, *J. Volcanol. Seismol.*, 2015, vol. 9, no. 4, pp. 242–257.
- Argus, D.F. and Gordon, R.G., No-net-rotation model of current plate velocities incorporating plate motion model NUVEL-1, *Geophys. Res. Lett.*, 1991, vol. 18, pp. 2039–2042.
<https://doi.org/10.1029/91GL01532>
- Balakina, L.M. and Moskvina, A.G., Characterization of the seismogenic process in the Aleutian Island Arc: I. Source relations of the large earthquakes of 1957, 1986, and 1996 in the Andreanof Islands, *Izv., Phys. Solid Earth*, 2008, vol. 44, no. 8, pp. 631–659.
- Balakina, L.M. and Moskvina, A.G., Characterization of the seismogenic process in the Aleutian Island Arc: II. The large earthquakes of February 4, 1965, and November 17, 2003, in the Rat Islands, *Izv., Phys. Solid Earth*, 2009, vol. 45, no. 3, pp. 199–224.
- Balakina, L.M. and Moskvina, A.G., Characterization of the seismogenic process in the Aleutian Island Arc: III. Earthquakes at the western and eastern margins of the Arc, *Izv., Phys. Solid Earth*, 2010a, vol. 46, no. 4, pp. 281–305.
- Balakina, L.M. and Moskvina, A.G., The tsunamigenic earthquake of April 1, 1946, in the Fox Islands (Aleutian Island Arc), *Izv., Phys. Solid Earth*, 2010b, vol. 46, no. 6, pp. 493–506.
- Chebrov, V.N., Droznin, D.V., Kugaenko, Yu.A., Levina, V.I., Senyukov, S.L., Sergeev, V.A., Shevchenko, Yu.V., and Yashchuk, V.V., The system of detailed seismological observations in Kamchatka in 2011, *J. Volcanol. Seismol.*, 2013, vol. 7, no. 1, pp. 16–36.
- Chebrov, D.V., Droznina, S.Ya., Senyukov, S.L., Shevchenko, Yu.V., and Mityushkina, S.V., Kamchatka and Commander Islands, in *Zemletryaseniya Rossii v 2015 godu* (Earthquakes in Russia in 2015), Obninsk: GS RAN, 2017a, pp. 67–73.
- Chebrov, D.V., Kugaenko, Yu.A., Abubakirov, I.R., Lander, A.V., Pavlov, V.M., Saltykov, V.A., and Titkov, N.N., The July 17th, 2017 $M_W = 7.8$ earthquake at the boundary of the Commander seismic breach (western part of the Aleutian Arc), *Vestn. KRAUNTs*, 2017b, vol. 35, no. 3, pp. 22–25.
- Cross, R.S. and Freymueller, J.T., Evidence for and implications of a Bering plate based on geodetic measurements from the Aleutians and Western Alaska, *J. Geophys. Res.*, 2008, vol. 113, p. B07405.
<https://doi.org/10.1029/2007JB005136>
- Droznin, D.V., Chebrov, D.V., Droznina, S.Ya., and Ototyuk, D.A., Automated estimation of instrumental seismic intensity in soft real time and use it within the service of urgent seismic reports in Kamchatka, *Seism. Prib.*, 2017, vol. 53, no. 3, pp. 5–19.

- Ekstrom, G., Stein, R.S., Eaton, J.P., and Eberhart-Phillips, D., Seismicity and geometry of a 110-km-long blind thrust fault: 1. The 1985 Kettleman Hills, California, earthquake, *J. Geophys. Res.*, 1992, vol. 97, pp. 4843–4864.
- Ekstrom, G., Nettles, M., and Dziewonski, A.M., The global CMT project 2004–2010: centroid-moment tensors for 13017 earthquakes, *Phys. Earth Planet. Inter.*, 2012, vol. 200, pp. 1–9.
- Fedotov, S.A., *Energeticheskaya klassifikatsiya Kurilo-Kamchatskikh zemletryasenii i problema magnitud* (Energy Classification of the Kuril-Kamchatka Earthquakes and the Problem of Magnitudes), Moscow: Nauka, 1972.
- Fukushima, Y. and Tanaka, T., The revision of “A new attenuation relation for peak horizontal acceleration of strong earthquake ground motion in Japan,” Fall Meeting of The Seismological Society of Japan, Abstracts, 1992, p. B18.
- Gaedicke, C., Baranov, B., Seliverstov, N., Alexeiev, D., Tsukanov, N., and Freitag, R., Structure of an active arc-continent collision area: the Aleutian-Kamchatka junction, *Tectonophysics*, 2000, vol. 325, no. 1, pp. 63–85.
- Geist, E.L., Childs, J.R., and Scholl, D.W., The origin of summit basins of the Aleutian Ridge: implications for block rotation of an arc massif, *Tectonics*, 1988, vol. 7, pp. 327–341.
- Gordeev, E.I., Pinegina, T.K., Lander, A.V., and Kozhurin, A.I., Beringia: seismic hazard and fundamental problems of geotectonics, *Izv., Phys. Solid Earth*, 2015, vol. 51, no. 4, pp. 512–521.
- Gusakov, V.K., Ground zero: megaequakes pose main threat to the safety of coastlines, *Sci. First Hand*, 2018, vol. 50, nos. 2–3.
- Herring, T.A., King, R.W., and McClusky, S.C., *GAMIT: GPS Analysis at MIT. Release 10.4*, Massachusetts: Institute of Technology, 2010.
- Kanamori, H. and Anderson, D.L., Theoretical basis of some empirical relations in seismology, *Bull. Seismol. Soc. Am.*, 1975, vol. 65, no. 5, pp. 1073–1095.
- Kogan, M.G., Frolov, D.I., Vasilenko, N.F., Freymueller, J.T., Steblou, G.M., Ekström, G., Titkov, N.N., and Pрыtkov, A.S., Plate coupling and strain in the far western Aleutian arc modeled from GPS data, *Geophys. Res. Lett.*, 2017, vol. 44, pp. 3176–3183.
- Lallemant, H.G.A. and Oldow, J.S., Active displacement partitioning and arc-parallel extension of the Aleutian volcanic arc based on Global Positioning System geodesy and kinematic analysis, *Geology*, 2000, vol. 28, no. 8, pp. 739–742.
- Lander, A.V., Bukchin, B.G., Droznin, D.V., and Kiryushin, A.V., Tectonic position and source parameters of the Khailin (Koryak) earthquake of March 8, 1991: does the Beringia plate exist?, in *Vychislitel'naya seismologiya* (Computational Seismology), vol. 26, Moscow: Nauka, 1994, pp. 103–122.
- Lander, A.V., Levin, V.E., and Titkov, N.N., Present-day movements of the Commander microplate from seismological and GPS data, *Vulkanizm i geodinamika: materialy IV Vserossiiskogo simpoziuma po vulkanologii i paleovulkanologii* (Volcanism and Geodynamics: Proc. IV All-Russian Symp. on Volcanol. Paleovolcanol.), Petropavlovsk-Kamchatskii, 2009, pp. 621–624.
- Lay, T., Ye, L., Bai, Ye., Cheung, K.F., Kanamori, H., Freymueller, J., Steblou, G.M., and Kogan, M.G., Rupture along 400 km of the Bering Fracture Zone in the Komandorsky Islands earthquake (M_W 7.8) of 17 July 2017, *Geophys. Res. Lett.*, 2017, vol. 44, no. 24, pp. 12161–12169. <https://doi.org/10.1002/2017GL076148>
- Levin, V.E., Bakhtiarov, V.F., Pavlov, V.M., Titkov, N.N., and Serovetnikov, S.S., Geodynamic studies of the April 20(21), 2006 Olyutorskoe earthquake based on observations by the Kamchatka GPS network, *J. Volcanol. Seismol.*, 2010, vol. 4, no. 3, pp. 193–202.
- Levin, V.E., Bakhtiarov, V.F., Titkov, N.N., Serovetnikov, S.S., Maguskin, M.A., and Lander, A.V., Monitoring and studying the present-day movements of the Earth's crust in Kamchatka, in *Seismologicheskie i geofizicheskie issledovaniya na Kamchatke* (Seismological and Geophysical Studies in Kamchatka), Petropavlovsk-Kamchatskii: Novaya kniga, 2012, pp. 188–210.
- Lobkovsky, L.I., Baranov, B.V., Dozorova, K.A., Mazova, R.Kh., Kisel'man, B.A., and Baranova, N.A., The Komandor seismic gap: earthquake prediction and tsunami computation, *Oceanology*, 2014, vol. 54, no. 4, pp. 519–531.
- Mackey, K.G., Fujita, K., Gunbina, L.V., Kovalev, V.N., Imaev, V.S., Kozmin, B.M., and Imaeva, L.P., Seismicity of the Bering Strait region: evidence for a Bering block, *Geology*, 1997, vol. 25, no. 11, pp. 979–982.
- Mazova, R.K., Baranov, B.V., Lobkovsky, L.I., Baranova, N.A., Dozorova, K.A., and Chaykina, O.N., Numerical model study of tsunami generated by potential earthquake within the Komandorsky seismic gap in the western Aleutian Island Arc, *Sci. Tsunami Hazards*, 2013, vol. 32, no. 3, pp. 131–155.
- McCaffrey, R., Oblique plate convergence, slip vectors, and forearc deformation, *J. Geophys. Res.*, 1992, vol. 97, no. B6, pp. 8905–8915. <https://doi.org/10.1029/92jb00483>
- McCann, W., Nishenko, S.P., Sykes, L.R., and Krause, J., Seismic gaps and plate boundaries: seismic potential for major boundaries, *Pure Appl. Geophys.*, 1979, vol. 117, pp. 1082–1147.
- Medvedev, S.V., Sponheyer, W., and Kárník, V., *Shkala seismicheskoi intensivnosti MSK-64* (Macroseismic Intensity Scale MSK-64), Moscow: MGK AN SSSR, 1965.
- Okada, Y., Surface deformation due to shear and tensile faults in a half-space, *Bull. Seismol. Soc. Am.*, 1985, vol. 75, no. 4, pp. 1135–1154.
- Papazachos, B.C., Scordilis, E.M., Panagiotopoulos, D.G., Papazachos, C.B., and Karakaisis, G.F., Global relations between seismic fault parameters and moment magnitude of earthquakes, *Bull. Geol. Soc. Greece*, 2004, vol. 34, pp. 1483–1489.
- Pavlov, V.M. and Abubakirov, I.R., The algorithm for calculating the seismic moment tensor of strong earthquakes from regional broadband seismograms of body waves, *Vestnik KRAUNTS. Nauki Zemle*, 2012, vol. 20, no. 2, pp. 149–158.
- Ruppert, N.A., Lees, J.M., and Kozyreva, N.P., Seismicity, earthquakes and structure along the Alaska-Aleutian and Kamchatka-Kurile subduction zones: a review, in *Volcanism and Subduction: The Kamchatka Region*, AGU Geophysical Monograph Series, 2007, vol. 172, pp. 129–144.

Ryan, H.F. and Scholl, D.W., Geologic implications of great interplate earthquakes along the Aleutian Arc, *J. Geophys. Res.*, 1993, vol. 98, no. B12, pp. 22135–22146. <https://doi.org/10.1029/93jb02451>

Seliverstov, N.I., *Stroenie dna prikamchatskikh akvatorii i geodinamika zony sochleneniya Kurilo-Kamchatskoi i Aleutskoi ostrovnykh dug* (The Seafloor Structure in the Region of Kamchatka and the Geodynamics of the Junction zone of the Kuril-Kamchatka and Aleutian Island Arcs), Moscow: Nauchnyi mir, 1998.

Sykes, L.R., Aftershock zones of great earthquakes, seismicity gaps, and earthquake prediction for Alaska and Aleutians, *J. Geophys. Res.*, 1971, vol. 76, no. 32, pp. 8021–8041.

Thingbaijam, K.K.S., Mai, M.P., and Goda, K., New empirical earthquake source-scaling laws, *Bull. Seismol. Soc. Am.*, 2017, vol. 107, no. 5, pp. 2225–2246.

Toda, S., Stein, R.S., Sevilgen, V., and Lin, J., Coulomb 3.3 Graphic-rich deformation and stress-change software for earthquake, tectonic, and volcano research and teaching—user guide, U.S. Geological Survey Open-File Report 2011-1060. <http://pubs.usgs.gov/of/2011/1060/>.

Wells, D.L. and Coppersmith, K.J., New empirical relationships among magnitude, rupture length, rupture width, rupture area, and surface displacement, *Bull. Seismol. Soc. Am.*, 1994, vol. 84, no. 4, pp. 974–1002.

Translated by M. Nazarenko